

UNIVERSITÀ DEGLI STUDI DI TORINO

SCUOLA DI SCIENZE DELLA NATURA

Corso di Laurea Magistrale in Fisica



Tesi di Laurea Magistrale

**TEST OF THE BEAM EFFECT ON  
VACUUM ARC OCCURRENCE IN A  
HIGH-GRADIENT ACCELERATING  
STRUCTURE FOR THE CLIC  
PROJECT**

Relatore:

Prof. Martino Gagliardi

Co-relatore:

Dr. Frank Tecker (CERN)

Candidato:

Eugenio Senes

Controrelatore:

Prof. Ferruccio Balestra

Anno Accademico 2015/2016

Considerate la vostra semenza:  
fatti non foste a viver come bruti,  
ma per seguir virtute e canoscenza.

Dante, *La Divina Commedia*  
Canto XXVI

# Abstract

A new generation of lepton colliders capable of reaching TeV energies is presently under development, and to succeed in this task it is necessary to show that the technology for such a machine is available. The Compact Linear Collider (CLIC) is a possible design option among the future lepton collider projects. It consists of two normal-conducting linacs. Accelerating structures with a gradient of the order of 100 MV/m are necessary to reach the required high energies within a reasonable machine length. One of the strictest requirements for such accelerating structures is a relatively low occurrence of vacuum arcs.

CLIC prototype structures have been tested in the past, but only in absence of beam. In order to proof the feasibility of the high gradient technology for building a functional collider, it is necessary to understand the effect of the beam presence on the vacuum breakdowns. Tests of this type have never been performed previously.

The main goal of this work is to provide a first measurement of the breakdown rate with beam in the accelerating cavity. The setup, the experimental procedure and the results of the tests executed on a prototype cavity for the Main Beam of CLIC are described.

The test were executed at CERN in the CLIC Test Facility 3 (CTF3), which houses a 12 GHz X-band Test Stand (XBOX). The XBOX supplies the radio-frequency power to the cavity prototype, while the beam is provided by the electron linac of the CTF3, reconfigured to produce a Main Beam-like pulse. A comparison between results obtained without beam and with different beam configurations will be presented, in an attempt to understand the beam effect on the breakdown rate. Moreover, future developments to improve the experimental setup and the operation of the tests stand will be proposed, based on the experience gained on high gradient testing with beam. This will be useful in case the experiment is repeated to complement and extend the results of this work.

# Italian abstract

È in fase di progetto una nuova generazione di acceleratori di leptoni capaci di raggiungere energie dell'ordine del TeV. È tuttavia necessario mostrare la fattibilità, verificando che sia accessibile la tecnologia necessaria a costruire simili macchine.

Il Compact Linear Collider (CLIC) è uno dei possibili progetti per un acceleratore lineare di leptoni, composto da due acceleratori lineari normalmente conduttori. Per raggiungere le alte energie del centro di massa richieste, conservando allo stesso tempo una lunghezza ragionevole della macchina acceleratrice, sono necessarie cavità di accelerazione con gradienti dell'ordine dei 100 MV/m. Uno dei parametri più stringenti per queste componenti è una occorrenza relativamente bassa di archi voltaici.

Prototipi di cavità acceleratrici per CLIC sono già stati testati in passato, ma solo in assenza di fascio. Per mostrare che la tecnologia della accelerazione ad alto gradiente è affidabile, è necessario comprendere quale sia l'effetto della presenza del fascio sull'innesto degli archi voltaici. Test con la presenza del fascio non erano mai stati effettuati fino ad ora.

L'obiettivo principale di questo lavoro è fornire la prima misura del rate di innesto degli archi voltaici in una cavità acceleratrice in presenza di fascio. Verranno descritti l'apparato, le procedure sperimentali e i risultati ottenuti dai test eseguiti su un prototipo di cavità acceleratrice da impiegare successivamente per il fascio principale di CLIC.

I test sono stati eseguiti al CERN nella CLIC Test Facility 3 (CTF3), dove è installato un setup di test per radiofrequenza ad alta potenza operante a 12 GHz (detto XBOX, X-band Test Stand). L'XBOX fornisce la radiofrequenza alla cavità in esame, mentre il fascio di elettroni impiegato proviene dal linac della CTF3, configurato per produrre un fascio simile al Main Beam di CLIC. Verrà presentata una comparazione tra i risultati ottenuti in assenza di fascio e con differenti configurazioni di fascio, al fine di comprendere l'effetto sul rate di innesto degli archi voltaici. Inoltre verranno proposti possibili futuri sviluppi sia per il miglioramento del setup sperimentale, sia per un perfezionamento delle procedure di test. L'esperienza acquisita durante lo sviluppo di questo lavoro e i conseguenti spunti saranno utili nel caso l'esperimento venisse ripetuto, per completare ed estendere i risultati ottenuti finora.

# Contents

<b>1</b>	<b>Introduction</b>	<b>1</b>
1.1	Generalities on colliders . . . . .	2
1.2	The CLIC project and the CTF3 facility . . . . .	3
1.2.1	Physics and staging . . . . .	4
1.2.2	Main parameters and main issues . . . . .	5
1.2.3	CTF3 . . . . .	8
<b>2</b>	<b>Accelerating structures</b>	<b>9</b>
2.1	Travelling wave accelerating structures . . . . .	9
2.1.1	Reminder of Electromagnetism . . . . .	9
2.1.2	Periodic accelerating structures . . . . .	11
2.1.3	Synchronous particle acceleration . . . . .	12
2.1.4	Figure of merit for accelerating structures . . . . .	13
2.2	High power limits and scaling laws . . . . .	14
2.2.1	Field emission law . . . . .	14
2.2.2	High power limits . . . . .	16
2.2.3	Power flow based criteria . . . . .	17
2.2.4	The modified Poynting vector $S_c$ . . . . .	17
2.3	The TD26CC structure for the Main Beam of CLIC . . . . .	19
<b>3</b>	<b>The breakdown process</b>	<b>22</b>
3.1	Detected effects of breakdowns in accelerating cavities . . . . .	22
3.2	Vacuum arc process description . . . . .	24
3.3	Breakdown rate scaling law . . . . .	25
3.4	Influence of the conditioning process . . . . .	27
<b>4</b>	<b>Motivation of the experiment</b>	<b>28</b>
<b>5</b>	<b>Experimental setup</b>	<b>31</b>
5.1	Linac and dogleg . . . . .	31
5.2	RF power production . . . . .	36
5.2.1	The X-Box1 at CERN . . . . .	36
5.3	DAQ & RF control systems . . . . .	38
5.3.1	Hardware . . . . .	38
5.3.2	Online triggers . . . . .	39
5.4	Other systems . . . . .	40

## CONTENTS

---

5.5	Operation of the setup . . . . .	41
5.5.1	Linac operation . . . . .	41
5.5.2	Xbox operation . . . . .	41
<b>6</b>	<b>Vacuum arc detection and localisation</b>	<b>43</b>
6.1	Offline selection of the events . . . . .	43
6.1.1	Data collected from the PXI . . . . .	43
6.1.2	Power spikes detection . . . . .	43
6.1.3	Pulse compressor tuning issues . . . . .	44
6.1.4	The metric . . . . .	46
6.1.5	Power back-off failure . . . . .	47
6.1.6	Additional criteria for runs with beam . . . . .	48
6.2	Time and space positioning of the breakdowns . . . . .	48
6.2.1	Edge method . . . . .	48
6.2.2	Correlation method . . . . .	49
6.2.3	Comparison of the two methods . . . . .	50
6.2.4	Time to space conversion . . . . .	54
6.3	Final data selection . . . . .	54
<b>7</b>	<b>Results and future developments</b>	<b>57</b>
7.1	Measurement summary . . . . .	57
7.1.1	Input power levels . . . . .	57
7.1.2	Beam pulse parameters . . . . .	59
7.2	Breakdown rate measurement results . . . . .	59
7.3	Breakdown distribution . . . . .	63
7.3.1	A model for the breakdown distribution . . . . .	63
7.3.2	Measurement results . . . . .	64
7.4	Beam induced RF . . . . .	67
7.5	Conclusions . . . . .	68
7.6	Further developments . . . . .	68
<b>List of Abbreviations</b>	<b>70</b>	
<b>List of Figures</b>	<b>71</b>	
<b>List of Tables</b>	<b>75</b>	
<b>Bibliography</b>	<b>76</b>	

# Chapter 1

## Introduction

Particle accelerators occupy a key role both in fundamental research and in all the applications and industrial processes that use technology and processes developed initially for the elementary research.

In fundamental research, accelerators are crucial to inquire the world at the elementary particle scale. But also the contribution given to the other sciences must not be neglected. In fact a number of examples could be named among the spin-offs of accelerator science, the most notable nowadays is the enormous progress of nanosciences in the last decade. This was made possible by the availability of high-brilliance synchrotron light sources, that were achievable thanks to the experience developed in the production of high quality electron beams. In the same way inquiring a much smaller scale requires machines involving higher energies. Hence in this perspective the continuous development of accelerators for the physical research is a fundamental requirement to assure that the cutting-edge technology of today turns into the "labware" of tomorrow for all the other sciences and industry.

Going back to the particle scale, at the moment the most successful model to explain the behaviour of the elementary particles is the *Standard Model*, which is however not able to answer all the questions still open in particle physics. A milestone in favour of the Standard Model was the observation of the Higgs Boson in 2012 [1, 2], which was made possible by the construction of the *Large Hadron Collider* at CERN[3]. However the full understanding of the physics at the particle scale still needs to be achieved. Partially this will be realised with the continued data taking of the LHC, but the International Committee for Future Accelerators (ICFA) considers that the results of LHC need to be complemented by the results of a lepton collider in the TeV-range [4].

The reason for this is that, according to the standard model, the hadrons are particles composed of quarks, that are continuously interacting by exchanging gluons. Collisions at high energy happen between partons (quark or gluons). In addition, there is no way to know *a priori* the energy of the partons involved, so it is impossible to know which will be the energy of the collision. For example it is improbable for a parton-parton collision at the LHC (where the energy in the proton-proton collision centre-of-mass is 14 TeV) to overcome 1-2 TeV [5].

On the other hand, the leptons are pointlike particles, so the interaction is directly involving the two accelerated particles.

This key difference in the behaviour of leptons and hadrons makes hadron colliders *machines for discovery*, because it involves all the possible processes that can take place in a wide range of energies, and the lepton machines *machines for precision*, because the reduced number of possible processes makes the observation of the events of interest much easier.

## 1.1 Generalities on colliders

According to the beam setup two kinds of accelerators can be distinguished:

1. Fixed target: where a beam is colliding with a non-moving target. The energy in the centre-of-mass is  $E_{CM} \propto \sqrt{E_{BEAM}}$
2. Colliders: where two beams are accelerated in opposite directions and then made to collide with each other. In the case of equal beam energy, in the centre-of-mass  $E_{CM} = 2E_{BEAM}$

Therefore it is easy to see that the collider topology is preferable to reach a high centre-of-mass energy.

The rate of observation of a particular interaction process A is given by

$$\frac{dN(A)}{dt} = \mathcal{L} \sigma(A) \quad (1.1)$$

where  $\sigma$  is the process cross-section, which depends on the physics of the process A itself, and  $\mathcal{L}$  is the luminosity, which depends entirely on the accelerator. Therefore the figure of merit for accelerators is the luminosity, which is given by

$$\mathcal{L} = \frac{H_d}{4\pi} \frac{N^2}{\sigma_x \sigma_y} n_b f_r \quad (1.2)$$

where  $N$  is the number of particles per bunch,  $\sigma_x$  and  $\sigma_y$  are the beam dimensions r.m.s. in the horizontal and vertical plane,  $n_b$  is the number of bunches,  $f_r$  is the collision frequency of the bunches and  $H_d$  is a correction factor that takes in account the non-ideality of the collision, such as crossing angle, collision offset, hour glass effect, non Gaussian beam profile and so on.

Reaching luminosities as high as possible is essential when the process to be studied are rare. This is achieved differently according to the design of the accelerator in use:

- linear accelerators (linacs) have a low repetition frequency, typically lower than hundreds of Hz, and the beam is passing through the accelerating structure just once.
- circular accelerators (typically synchrotrons) have a higher repetition frequency, up to tens of kHz, and are keeping the particle beam in orbit for many turns.

After this distinction one could be led to think that the circular machine has a clear advantage when high luminosity is desired, but raising the energy of the beam becomes problematic: in fact the power lost in a circular collider due to the emission of synchrotron radiation scales according to the following expression

$$P \propto \frac{1}{\rho^2} \frac{E^4}{m_0^4} \quad (1.3)$$

where  $\rho$  is the bending radius of the machine,  $E$  is the particle energy and  $m_0$  is its rest mass. The power loss becomes very important for electrons and positrons. As can be noted in Table 1.1, the energy loss per turn is a relevant fraction of the beam energy, e.g. for the LEP collider, at the highest energy per beam of 104.5 GeV, more than 3 GeV were lost per turn. To raise the beam energy and reduce the energy loss, the radius of circular machines escalates quickly. A simple scaling from LEP shows that in order to reach the centre-of-mass energy of 3 TeV, the circumference should be increased to thousands of kilometers [6]. To solve the issue, the development of new lepton colliders is focusing on two different solutions:

1. Use muons instead of electrons: this innovative approach reduces the power lost because of the higher mass of the muon compared to the electron, but one has to deal with the short lifetime of muons, which is roughly  $2 \mu s$  in their rest frame.
2. Limit the losses caused by synchrotron radiation, either by increasing the bending radius or abandoning the circular topology for the linear one.

It has to be noted that the muon technology is rather new and still needs to be fully developed, while the linear accelerator technology profits of the progress achieved in the last half century mainly at CERN, SLAC and KEK.

In this perspective a number of projects are under study at the moment, of which the most ambitious are FCC-ee, *Future Circular Collider*, ILC, *International Linear Collider*, and CLIC, *Compact Linear Collider*. The first one consists of a circular collider which is supposed to be placed in a 80-100 km long tunnel before the installation of the FCC-hh, the others are linacs even if based on completely different technologies and solutions. A comparison of the features of these projects in the final stage is presented in Table 1.1, together with LEP as an example of a circular lepton collider.

Furthermore a recent interest arose in more compact technologies, e.g. plasma acceleration techniques, but the reliability of such designs still needs to be proven in the perspective of creating a fully functional machine that goes beyond the demonstration of the working physical principle.

## 1.2 The CLIC project and the CTF3 facility

The *Compact Linear Collider* is the project for a linear electron-positron collider capable of reaching a centre-of-mass collision energy of 3 TeV and a

Parameter	LEP2	FCC-ee	CLIC		ILC
$\sqrt{s}$ [GeV]	209	350	500	3000	500
$\mathcal{L}_{peak}$ [ $10^{34} \text{ cm}^{-2} \text{ s}^{-1}$ ]	0.012	1.3	2.3	5.9	1.8
Total length [km]	26.7	100	13	48.4	31
$E_{acc}^{loaded}$ [MV/m]	5 - 9	10 - 20	80	100	31.5
Bunch population [ $10^9$ ]	105	170	6.8	3.72	500
Bunch spacing [ns]		4000	0.5	0.5	554
Collision rate [Hz]		$\approx 3000$	50	50	5
$\epsilon_x^* / \epsilon_y^*$ [ $\mu\text{m}/\text{nm}$ ]		0.68/0.68	2.4/25	0.66/20	10/35
$\sigma_x^* / \sigma_y^*$ [nm]		3600/70	202/2.3	40/1	474/5.9
Energy loss [GeV turn $^{-1}$ ]	3.34	7.55	-	-	-
AC Power [MW]	120	$\approx 300$	271	582	163

Table 1.1: Comparison of two circular machines, LEP[7, 8] with FCC-ee[9, 10] with two projects for linear machines: the first and last stage of the CLIC implementation [11] and the ILC[12]

luminosity of  $2 \times 10^{34} \text{ cm}^{-2} \text{ s}^{-1}$  in the final stage.

### 1.2.1 Physics and staging

The machine is designed to be built in 3 stages, with a final energy of 3 TeV.

Since the Conceptual Design Report (CDR)[11] was released just before the discovery of the Higgs boson, the centre-of-mass energy stages have been reshaped in order to be able to access interesting measurements. For a given centre-of-mass energy stage, the energy can be modified by  $\simeq 30\%$  with limited loss of performance [13], allowing an eventual retuning of the energy of the stages following the results of the LHC physics campaign.

The energy staging has been chosen with the idea to access the Higgs and top physics since the first stage [14, 15].

In the first stage at 380 GeV the measurements on the Higgs physics can be conducted through Higgsstrahlung and WW-fusion processes, thereby providing accurate model-independent measurements of Higgs couplings to bosons and fermions[16]; the top physics measurements will focus on the  $t\bar{t}$  pair production threshold in the vicinity of  $\sqrt{s} = 350$  GeV.

The second stage is proposed at 1.5 TeV and allows one to access new physics phenomena and additional properties of the Higgs boson and the top quark, such as Higgs self-coupling and rare Higgs branching ratios.

The third stage is proposed at 3 TeV and will give direct access to pair-produced particles with mass up to 1.5 TeV or single particles with mass up to 3 TeV. This stage is particularly interesting as test for the Beyond Standard Model theories, since such high energy in a lepton machine makes the observation of new particles much easier than in the LHC.

A further adaptation of these steps is possible after the publication of the

results of the Run 2 of the LHC. In any case the advantage of a linear machine in this sense is that the final energy can be reshaped by modifying the total length of the machine. Figure 1.1 shows the footprint of a possible CLIC built in the Geneva area, in order to give an idea of the size of that kind of facility compared to LHC.

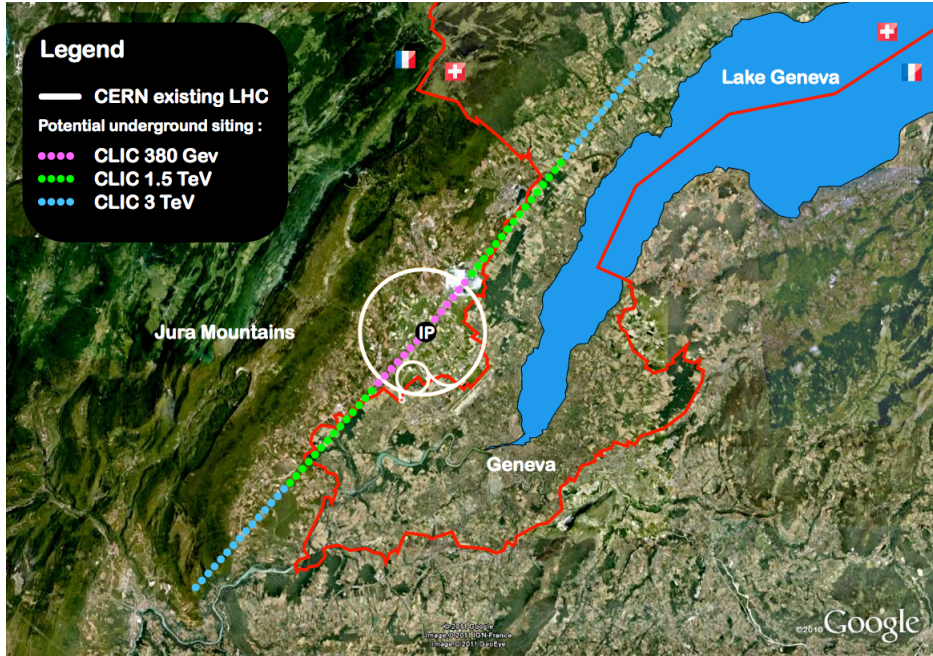


Figure 1.1: Map of the CLIC facility, if implemented in the Geneva area.

### 1.2.2 Main parameters and main issues

The realisation of a machine like CLIC implies many technological challenges in order to keep the power consumption and the dimension limited while matching the design goal parameters. These challenges have been faced by developing the novel *two-beam acceleration scheme*, which uses a high-current and low-energy beam, the *Drive Beam*, in order to generate the radio-frequency (RF) power to accelerate a low-current and high-energy beam used for the experiments, named *Main Beam*.

The Drive Beam is produced using a dedicated linac, and then the current is multiplied using a delay loop and two recombination rings, reaching a combination factor of  $2 \times 3 \times 4 = 24$ . This topology generates the beam with a final bunch frequency of 12 GHz. It is essential to reach the highest possible efficiency in the Drive Beam production, in order to shrink the power consumption to the smallest possible value. To reach this goal the acceleration in the linac is performed using the accelerating cavities in fully-loaded mode [17].

While the biggest challenge for the Drive Beam to reach the necessary stable high current, for the Main Beam the hardest challenge is generating a beam with the smallest possible size, in order to increase the luminosity of the

machine as much as possible.

The Main Beam is produced in a separate facility, where a DC-photo gun system provides the initial polarised electron beam. The positron beam is generated by another electron beam hitting a target. Once both beams have been produced, they are sent to the next accelerating stages, which are composed of linacs to raise the beam energy and of damping rings to reduce the emittances.

The detailed description of the Main Beam production and the Drive Beam recombination process can be found in [11]. The working principle has been demonstrated in the CTF3 [18].

Both beams are sent to the common tunnel where the Two-beam modules are installed. The Two-beam module is composed of two principal sections, the PETS, *Power Extraction and Transfer Structures*, and the accelerating structures for the Main Beam, as shown in Fig. 1.3. The Drive Beam passes through the PETS and gets decelerated. As product of the deceleration a pulse of RF power is produced, which is transferred by a waveguide network and used to accelerate the Main Beam. In this way an efficient acceleration of the Main Beam up to the desired energy for the experiments is possible.

Figure 1.2 shows the layout of the CLIC facility in the final energy stage.

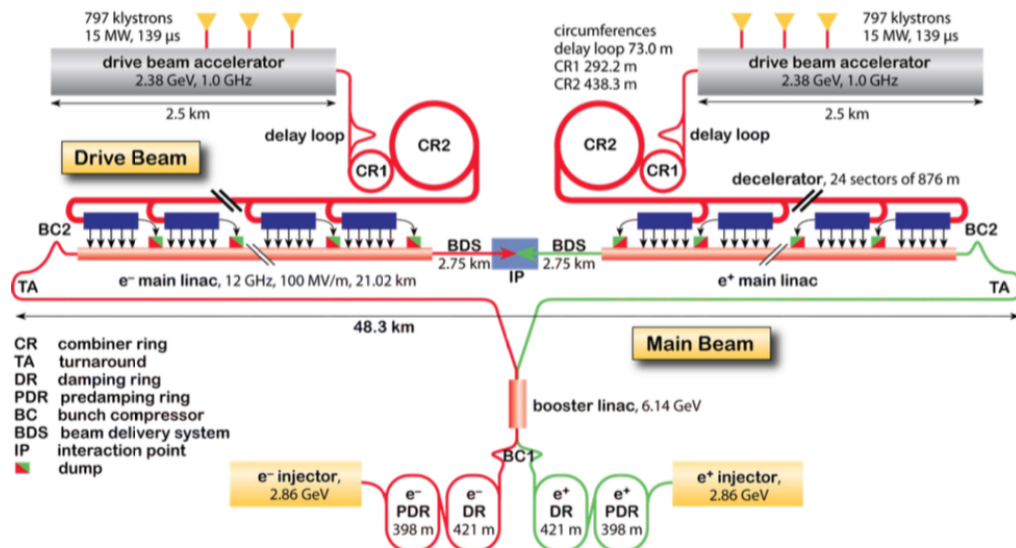


Figure 1.2: Layout of the final stage of CLIC.

There are many issues that can affect the performance of a machine like CLIC, and need to be analysed carefully since no similar machine has been built so far.

The main issues are:

1. 100 MV/m accelerating gradient: this requirement comes from the final energy of 3 TeV and the requirement of a maximum length of 50 km.



Figure 1.3: Design of a Two-beam module.

2. Breakdown rate  $< 3 \times 10^{-7}$  breakdowns per pulse per meter: this limitation comes from the limit on design luminosity loss in case of breakdown. This is the aim of this work and will be stressed in detail later.
3. Transverse wakefields limitation: wakefields have to be considered because of the short bunch spacing in the bunch train. If not limited, they are a serious issue to the luminosity.
4. Powering the accelerating structures: the klystrons on the market are not able to produce a high-power RF-pulse 150-200 ns long with a high efficiency. In order to achieve a high efficiency, it is possible to use klystrons equipped with RF pulse compression systems. This option is an alternative for the first energy stage of CLIC. For higher energies, the Drive Beam option is more cost efficient.
5. Generate the drive beam with the highest efficiency in order to contain the power consumption. Also the efficiency of the power transfer between the beams is a key issue in order to reach the energy goal.
6. Extremely small beam emittance and size: in order to match the luminosity goal with the typical low repetition rate of a linac it is necessary to squeeze the beam as much as possible, reaching the goal of 40 and 1 nm at the interaction point in the horizontal and vertical plane. This

requirement includes the realisation of a nanometric alignment and vibration stabilisation system.

The parameters in Table 1.2 have been chosen in order to match the design parameters reported in Table 1.1 for the top design energy.

Description	CLIC 3 TeV
Peak luminosity [cm <sup>-2</sup> s <sup>-1</sup> ]	2.0x10 <sup>34</sup>
Total site length [km]	48.4
Loaded accelerating gradient [MV/m]	100
Main LINAC RF frequency [GHz]	12
Number of particles per bunch	3.7x10 <sup>9</sup>
Bunch separation [ns]	0.5
Bunches per train	312
Beam pulse duration [ns]	156
$\epsilon_x^* / \epsilon_y^*$ [ $\mu\text{m}$ ]/[nm]	0.66/20
$\sigma_x^* / \sigma_y^*$ [nm]	40/1

Table 1.2: CLIC main parameters in the final stage

### 1.2.3 The CLIC Test Facility 3

To prove that the CLIC scheme is a feasible and a reliable technology to build a functional collider, a number of tests have to be conducted since no accelerators using the Two-beam acceleration concept have been built. The CLIC Test Facility 3 has been built and operated at CERN in order to demonstrate experimentally:

- The feasibility of the Drive Beam generation with a frequency of 12 GHz, performing the beam recombination by means of a delay loop and a combiner ring for a total multiplication factor of  $2 \times 4 = 8$ .
- The RF power production using the PETS and investigate possible issues of the Two-beam scheme.

In addition, a branch of the linac was used to perform high-gradient tests with the beam presence inside the accelerating cavity, which is the topic of this work. A more detailed description of such branch will follow in Chap. 5.

# Chapter 2

## Accelerating structures

The accelerating structures are one of the key parts of a particle accelerator. Even though in the first accelerators the particle acceleration was achieved simply with fixed fields, this technique showed its limitations quite soon due to the impossibility to create arbitrary high DC voltages without being subjected to electrostatic discharges. The present conventional technology for particle acceleration is based on RF cavities, so reaching the highest possible acceleration within a reasonable accelerator length requires to push such technology to its highest performance. In the case of the CLIC project a key issue is to be able to produce cavities with an accelerating gradient of 100 MV/m, which is the cutting-edge value at the moment while keeping the breakdown rate limited.

In this chapter some generalities about the theory of accelerating cavities will be presented. The aim is to give the reader a theoretical introduction to better understand the description of the cavity under test.

### 2.1 Travelling wave accelerating structures

In this section some useful concepts and result of the electromagnetic theory will be recalled. For the sake of conciseness, the examples and the geometries presented will refer to travelling wave accelerating structures, since it is the only type of structure used in this work. The curious reader can find details on the untreated topics in [19, 20, 21] and in plenty of specialised books.

#### 2.1.1 Reminder of Electromagnetism

##### Maxwell's equations

It is well known that the propagation of the electromagnetic fields follow the Maxwell's equations, that in a medium are

$$\begin{aligned}\nabla \cdot \mathbf{D} &= \rho_{\text{free}} \\ \nabla \cdot \mathbf{B} &= 0 \\ \nabla \times \mathbf{E} &= -\frac{\partial \mathbf{B}}{\partial t} \\ \nabla \times \mathbf{H} &= \mathbf{J}_{\text{cond}} + \frac{\partial \mathbf{D}}{\partial t}\end{aligned}\tag{2.1}$$

where  $\mathbf{E}$  and  $\mathbf{B}$  are the electric and magnetic field in the vacuum,  $\rho_{\text{free}}$  is the free charge density in the medium,  $\mathbf{J}_{\text{cond}}$  is the conduction current density vector,  $\mathbf{D} = \epsilon \mathbf{E}$ ,  $\mathbf{B} = \mu \mathbf{H}$  and  $\mathbf{E} = \sigma \mathbf{J}_{\text{cond}}$ . The propagation in vacuum is described by the same equations and can be easily derived with an appropriate choice of the constants.

### Waveguides and resonant cavities

In some particular cases the confined propagation of electromagnetic waves is possible, and is commonly realised using a metal waveguide to direct all the energy in a single direction. In this section some useful results on the propagation in a waveguide will be stressed, while the full derivation can be found in literature [19, 22, 23].

The request of propagation in the direction of the axis of the waveguide can be traduced to the condition  $\mathbf{E} \times \mathbf{n} = 0$ , where  $\mathbf{n}$  is the local unit vector orthogonal to the surface, that means asking that no power is dissipated in the walls of the cavity by Joule effect since the electric field is normal to the surface anywhere and anytime.

Many solutions can be found to the problem, integrating the Maxwell's equations with the given boundary condition, but without entering in the calculations, the interesting solutions belong to two classes:

- **TM modes:** Transverse Magnetic modes, where the axial component of the magnetic field is null.
- **TE modes:** Transverse Electric modes, where the axial component of the electric field is null.

Every mode has a particular cutoff frequency, and will propagate only in case that the condition  $\omega > \omega_c$  is met (where  $\omega_c = 2\pi f_c$  and  $f_c$  is the cutoff frequency of the mode). The cutoff frequency of each mode depends mainly on the geometry of the guide utilised, and waves with a frequency lower than the cutoff frequency will be exponentially damped.

The major features of a waveguide are: the *phase velocity* is  $v_p = \frac{\omega}{k} > c$ ; the *group velocity* is  $v_g = \frac{\partial \omega}{\partial k} < c$ , as expected for the physical quantity representing the speed of propagation of the electromagnetic wave according to Relativity; the dispersion relation for a uniform waveguide can be expressed as

$$\omega^2 = \omega_c^2 + (k_0 c)^2 \quad (2.2)$$

where  $k_0$  is the wavenumber of the wave propagating in the vacuum.

The waveguides are a key building block of particle accelerators to deliver the RF power from the production equipment to the accelerating cavities. But they are not suitable for particle acceleration as they are. The reason is that to accelerate the particles the phase velocity of the RF has to be similar to the velocity of the beam, which cannot exceed the speed of light.

A particular case is represented by *Resonant Cavities*, which are in the simplest case closed waveguides at the terminations (e.g. a cylindrical cavity,

or *pillbox cavity*, is composed of a circular waveguide closed by two planes at the extremities). In resonant cavities the electromagnetic field can resonate according to the particular eigenfrequencies of the system, which are mainly dictated by the geometry. This process allows propagation of just a set of frequencies, just like in the waveguides, but a cavity operating at one of the eigenfrequency starts to accumulate energy because of the resonance. This mechanism is used in accelerating structures.

### 2.1.2 Periodic accelerating structures

To reduce the phase velocity into the structure, it is possible to load it with additional metallic walls placed orthogonally to the axis of the cavity. Such structures are named *Disk (or Iris) Loaded Accelerating Structures*. A schematic example is presented in Fig. 2.1

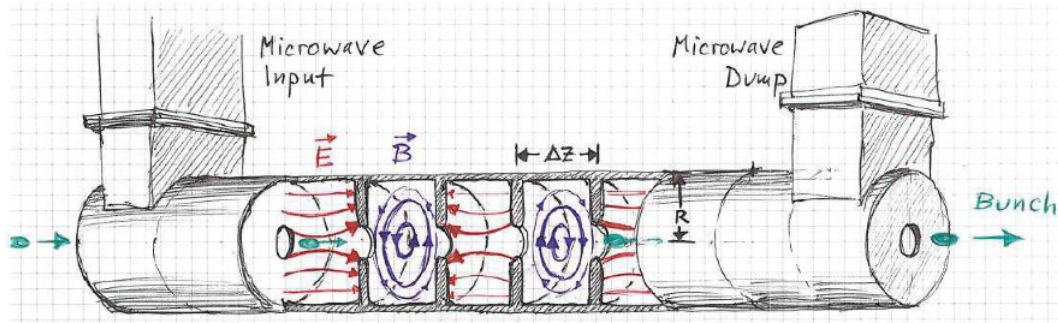


Figure 2.1: Scheme of a travelling wave, disk loaded accelerating structure. The drawings illustrates the input and output couplers, the disks loading the cavity and the beam passing through the irises. From [24]

The accelerating structure is composed of *cells*, which are connected by the *iris* to the adjacent cells. At the beginning and end of the structure two special cells form the input and output coupler for the RF. The role of the irises is to create a free path for the passage of the beam and allowing the propagation of the EM field from the input coupler to the output one. In the case of room temperature cavities the material normally used is copper, while for superconducting cavities the material can vary and also metallic cavities coated internally with a superconductive layer are a possibility.

From the field perspective, the fact that the accelerating structure is loaded with the disks changes the way that the EM waves propagate in the structure. The full mathematical description, is found in [19, 23], here simply a general idea of the process and of the relevant results is given.

The geometry of the accelerating structure can be seen as a cylindrical cavity loaded regularly with the disks. If as first approximation we consider an infinite structure, it is possible to use the *Floquet's Theorem*, that can be summarised as follows: "*In a given mode of an infinite periodic structure, the fields at two different cross sections that are separated by one period differ only*

by a constant factor, which in general is a complex number". This has two main implications: there are some regions of the spectrum of  $\omega$  that do not allow the waves to propagate, called *stopbands*, and others, called *passbands*, where the propagation is allowed with a *phase shift*  $\Delta\phi = k_0 d$ , where  $d$  is the length of the cell. The phase advance per cell is a particular parameter of every structure, and is defined in the design phase.

The waves that are allowed to propagate in such conditions are called *Space Harmonics*, and can be seen as an infinite number of waves propagating at the same frequency but with different wavenumbers. The dispersion relation becomes

$$\omega^2 = \omega_c^2 + c^2 \left( k_0 + \frac{2\pi n}{d} \right)^2 \quad (2.3)$$

where the principal wave of the mode has  $n = 0$  and the others have  $n$  according to the direction of propagation.

The phase velocity of the  $n$ -th harmonic becomes

$$\beta_n = \frac{\omega}{k_n c} = \frac{\beta_0}{1 + n\beta_0\lambda/d} \quad (2.4)$$

which allows to reach an arbitrary low phase velocity, as requested for the particle acceleration.

The comparison of the phase velocity of a waveguide and accelerating structure is presented in Fig. 2.2.

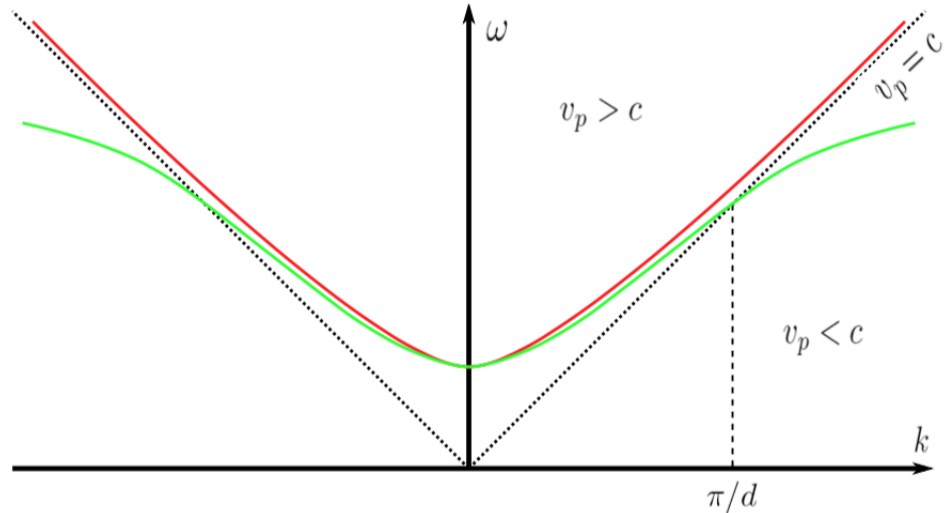


Figure 2.2: Brillouin diagram of a uniform waveguide (red) compared to a disk-loaded accelerating structure (green) [25]

### 2.1.3 Synchronous particle acceleration

A particle injected in an electromagnetic field in some conditions can gain energy at expense of the field, getting accelerated. This is realised in travelling-wave structures by injecting the particle at the right moment and ensuring that

the field and the particle have a similar speed. In this manner the particle can travel with the field with an energy gain given by

$$\Delta W = qV_0 \cos\phi \quad (2.5)$$

where  $q$  is the charge of the particle,  $V_0$  is the accelerating field and  $\phi$  is the relative phase between particle and RF field.

In order to deliver a constant energy gain to a charged particle it is necessary to shape the EM field matching two fundamental conditions:

1. The electromagnetic wave has to have a non-zero component in the direction of the motion of the particle
2. The phase velocity of a wave has to be similar to the particle velocity

the two condition cannot be met neither in free space, nor in simple waveguides, but travelling wave structures shape the electromagnetic field to propagate in the desired form.

#### 2.1.4 Figure of merit for accelerating structures

To characterize different accelerating structures, is necessary to rely on some significant quantities that can be derived from the geometry of the cavities. The most important figures of merit (FOMs) are the following (a number of different definitions are commonly used, here they are reported in accordance with [26]):

- **Quality factor**

$$Q_0 = \frac{\omega_0 U}{P_{loss}} \quad (2.6)$$

is a standard FOM for the resonant cavities, representing the stored energy  $U$  over the power dissipated  $P_{loss}$

- **Shunt impedance**

$$R = \frac{V_{acc}^2}{2P_{loss}} \quad [M\Omega] \quad (2.7)$$

represents the effectiveness of producing an axial voltage  $V_{acc}$  for a given power dissipated. For long cavities, where it is preferable to have a quantity that is independent from the length of the structure, the Shunt impedance per unit length  $Z$  is commonly used

$$Z = \frac{R}{L} \quad [M\Omega/m] \quad (2.8)$$

where  $L$  is the length of the cavity.

- **R over Q**

$$\frac{R}{Q} = \frac{(V_{acc})^2}{2\omega_0 U} \quad [M\Omega] \quad (2.9)$$

represents the relation between the accelerating field  $V_{acc}$  and the stored energy  $U$

- **Filling time (for travelling-wave structures)**

$$t_F = \int_0^L \frac{dz}{v_g(z)} \quad (2.10)$$

is time needed by the EM field to fill the structure

- **Power delivered to the beam**

$$P_B = \frac{I \Delta W}{q} \quad (2.11)$$

where  $I$  is the beam current and  $\Delta W$  is the energy gain

- **Beam loading ratio**

$$\epsilon_s = \frac{P_B}{P_{tot}} \quad (2.12)$$

represents the fraction of power supplied that is delivered to the beam

## 2.2 High power limits and scaling laws

The limiting factors for room-temperature high-gradient accelerators have been identified as *field emission* and *RF breakdown*. The former is the emission of electrons in the form of the so called "*Dark current*", that subtracts RF power, causes radiation and can produce wakefields; the latter is a limiting factor to the operation of accelerators and can damage the structures [27].

The understanding of these phenomena is particularly challenging and requires a mixture of notions of disciplines such as surface physics, metallurgy, fabrication processes, microwaves, beam dynamic and plasma physics. At the moment a satisfactory unified theory of the processes that take place during the breakdowns has not been found yet. The improvement of the structures is achieved using scaling laws for the high power limitations, that have been deducted from the experience and the experiments on the structures tested so far.

### 2.2.1 Field emission law

#### Emission from flat clean surface

The field emission law was theorised by Fowler and Nordheim in 1928 and rules the current emission from a metal with an intense electric field applied. The

derivation was carried out calculating the tunneling probability of electrons of the conduction band through the perfectly flat and clean surface of a metal. The applied electric field modifies the potential barrier, and the current density  $J_F$  of emitted electrons can be derived as the following, giving the *Fowler-Nordheim equation* [28]

$$J_F = \frac{1.54 \times 10^{-6} \times 10^{4.52\phi^{-0.5}} E^2}{\phi} \exp\left(-\frac{6.53 \times 10^9 \phi^{1.5}}{E}\right) \quad [A m^{-2}] \quad (2.13)$$

where  $\phi$  is the work function of the material and  $E$  is the applied electric field.

### Enhanced field emission

It is well known that almost any surface is never perfectly clean and flat, and also the fact that the roughness of the surface provokes an enhancement of the local electric field. This behaviour lead to the phenomenon known as *Enhanced Field Emission* (EFE), which major contributors are:

- Surface imperfections due to imperfect machining
- Metallic dust
- Molten craters after breakdowns
- Absorbed gas

These effects can create particular sites known as "emitters". It is a common praxis to define the field enhancement factor  $\beta$  to relate the electric field  $E$  to the microscopic one  $E_m$

$$E_m = \beta E \quad (2.14)$$

The  $\beta$  factors can be calculated according to the emitter's geometry [29] as shown in Fig. 2.3. Using Eq. 2.13, the current  $I_F$  emitted from EFE by an emitter site of area  $A$  becomes

$$I_F = \frac{1.54 \times 10^{-6} \times 10^{4.52\phi^{-0.5}} A \beta^2 E^2}{\phi} \exp\left(-\frac{6.53 \times 10^9 \phi^{1.5}}{\beta E}\right) \quad [A] \quad (2.15)$$

where  $\beta E$  is the local field,  $\phi$  is the work function of the material and  $A$  the area of the considered emitter.

In the RF case the average current emitted is given by similar calculations, averaging the electric field on an RF period [27].

Experimental evidence of the dark current emission have been detected by setups equipped with Faraday Cups, as in [30].

The emission of dark current seems to be a precursor of the breakdown process, even if the relationship between the two processes has not been clarified so far.



Figure 2.3: Field enhancement factors for simple geometries of metallic protrusions, plotted as function of geometrical features. From [29]

### 2.2.2 High power limits

In an historical perspective, the Kilpatrick's Critereon was the first attempt to create a high power limit for the vacuum breakdown valid both in DC and RF applications [31]. The model was based on the acknowledgement of the Field Emission, and suggesting that the vacuum arc was created by the cascade of secondary electrons ejected from the surface triggered by an initial ion bombardment. The main result was to find a law ruling the maximum electric field achievable without triggering a breakdown.

This critereon was reviewed many times up to now, because the experiments conducted nowadays show a field limit 7-8 times higher than Kilpatrick's prediction. This can be ascribed to different reasons: first of all the quality of the machining of the structures has increased considerably since the 1950's; in second instance Kilpatrick examined simple geometries, while real RF cavities are more complicated.

At the end of the 1980's J.D.Wang proposed a model based on micropromtrusion effect on the field and field emission, that involves the formation of a micro-plasma during the breakdown process. Also the Kilpatrick's limit was revised again in order to match the experimental results. [32, 33]

Further theories on the mechanism of breakdowns evolved, and will be mentioned in chapter 3.

The two scaling laws presented in the next two paragraphs are currently used in the design of modern accelerating structures.

### 2.2.3 Power flow based criteria

Other scalings have been proposed, like the phenomenological  $P/C$ -criterion, where  $P$  is the power flowing in the cavity and  $C$  the minimum iris circumference. It is straightforward to see that this is strongly related to the maximum surface electrical field, which is stronger for smaller irises. It has to be underlined that this is suitable just to travelling wave structures (TWS), since the power flow in standing wave structures (SWS) is close to zero.

In recent years a more advanced version of the scaling has been presented [34], which is quantified by

$$\frac{P\tau^{1/3}}{C} \quad (2.16)$$

where  $P$  is the power flow through the structure,  $\tau$  the pulse length and  $C$  the minimum iris circumference. This has also been formulated as  $(f \times P/C)^{0.5}$ , which is a quantity linear with the field [30].

Anyway, although these criteria are still in use today for the accelerating structure design, it needs to be found a more general criterion valid for any type of cavity.

### 2.2.4 The modified Poynting vector $S_c$

During the development of high-gradient normal conducting accelerating structures for the CLIC project, a new field quantity was developed, the *Modified Poynting Vector*  $S_c$ , that is suitable both for TWS and SWS [35].

The formulation is based on two assumptions: the breakdown process is determined by the accumulation of the pulses rather than the single pulse and the possible triggers of the breakdown can be induced by many processes that will be discussed later and are not relevant for the scaling law derivation.

A number of effects have to be taken into account (a simple geometry is considered, a cylindrical protrusion surmounted by a hemispherical cap):

#### Pulsed heating by field emission current

it is known that the field emission gets enhanced by the presence of the protrusion as described before. In this case the field enhancement factor can be expressed as  $\beta \simeq h/r$ , where  $h$  is the tip height and  $r$  is the cap radius. So the tip will emit a current according to the Fowler-Nordheim law Eq. 2.15, causing in first approximation the heating of the tip due to the ohmic heating as shown in Fig. 2.4. Assuming that the edge of the tip will be the most heated part, and using the heat conduction equation, it is possible to derive the emitted current to melt the tip, which for copper is found to be approximately  $36 \text{ A}/\mu\text{m}^2$  for a tip of  $1 \mu\text{m}$  height and a pulse of 100 ns. This is consistent with the findings in [36]. The  $\beta$  factor can be then derived, which is approximately between 40 and 60 considering a surface electric field in case of breakdown between 200 and 300 MV/m, according with the experimental results.



Figure 2.4: (a) Electric field distribution around the protrusion considered. (b) Field emitted current and power flow. In both the plots arrows indicate the direction of the field and the color code the absolute value of the field, mapped logarithmically.[35]

### Power flow near an emission site

The heating of the tip mentioned before requires a huge amount of energy, which can be supplied only by the RF power present into the cavity. This is described by the Poynting vector  $S_{RF} = E \times H_{RF}$ . As discussed before a current is established in the tip, and flows through, subtracting energy from the EM field in the surroundings of the tip. The current flows through the tip and leaves it at the edge, getting sprayed in the cavity according to the Fowler-Nordheim theory. Since any current flowing creates an associated magnetic field, the power flow due to the emission is given by  $S_{FN} = E \times H_{FN}$ .

The key point is that since the copper is a very good conductor, to provoke a notable ohmic heating of the tip, a significant power flow through the tip is necessary. This can be calculated evaluating the  $S_{FN}$  at a distance  $d = h$  from the edge of the tip, where the electric field is not perturbed anymore by the shape of the tip itself. This can be formulated as the condition

$$P_{RF} \geq P_{FN} \gg P_{loss} \quad (2.17)$$

where  $P_{loss}$  is the power lost for ohmic heating and  $P_{FN}$  the power flow through the tip.

Considering now the relative phase of the  $P_{RF}$  and of the  $P_{FN}$  it is possible to derive an expression for the power emitted from the tip in a copper cavity

$$P_{FN}(t) = A E_0^3 \sin^3 \omega t \exp\left(\frac{-62}{\beta E_0 \sin \omega t}\right) \quad (2.18)$$

where the work function of the copper  $\phi = 4.5 \text{ eV}$  has been used,  $A$  is the area of the conductor and  $\omega = 2\pi f$  is the angular velocity.

The RF power can be divided in real and imaginary part, with a phase shift of  $90^\circ$ . The real part is the energy propagating into the structure only

and the imaginary part is the energy stored in the cavity both magnetically or electrically as it is the case in every resonant cavity. Since the active power flow is more efficient than the reactive one in providing power for the field emission, a weighting factor  $g_c$  is introduced. The values of  $g_c$  vary slowly as function of the local electric field. For practical reasons all the simulation codes work using the complex Poynting vector  $\bar{S}$ , the precedent reasoning can be adapted to follow this practice, using the *Modified Poynting Vector*

$$S_c = \text{Re}\{\bar{S}\} + g_c \text{Im}\{\bar{S}\} \quad [\text{W}/\mu\text{m}^2] \quad (2.19)$$

Since this quantity can be calculated in any point of a structure, this allows to identify in advance the regions which are more sensitive to the breakdown process. The rule of thumb given by the experience says that this quantity should not exceed the value of  $5 \text{ W}/\mu \text{ m}^2$  to have a breakdown rate smaller than  $1 \times 10^{-6} \text{ bpp m}^{-1}$  with a pulse length of 200 ns.

This quantity has been used to design all the latest generations of CLIC structures, including the one tested in this work.

## 2.3 The TD26CC structure for the Main Beam of CLIC

After introducing in the previous section the general laws that regulate the operation of the TWS, the structure under test in this work, the TD26CC, will now be presented. The name stands for Tapered, Damped, 26-cells active cells structure with Compact Couplers.

One has to bear in mind that in the design of the real cavities, it is almost never possible to use the general laws described in precedence because of the high complexity of the geometry. A great work of design and simulation is necessary, and is carried out with complex numerical simulations. This section will present a summary of the parameters and features of the cavity; the details can be found in [11, 37, 38].

As pointed out in [11], the main constraints in the structures for the main beam linac are

1. Maximum surface electric field:  $E_{surf}^{max} < 260 \text{ MV/m}$
2. Pulsed surface heating:  $\Delta T^{max} < 56 \text{ K}$
3. Power density:  $P_{in}/C\tau_p^{1/3} < 18 \text{ MW/mm ns}^{1/3}$

These limitations, together with the parameters listed in section 1.2.2, lead to the current design after a careful optimisation and tradeoff of the parameters. The main parameters are reported in Table 2.1

The structure is fabricated by stacking machined copper disks that are brazed together with a particular procedure that has been elaborated in order to achieve the highest mechanical precision possible in the alignment of the

Average loaded accelerating gradient	100 MV/m
Frequency	12 GHz
RF phase advance per cell	$2/3\pi$ rad
Average iris radius to wavelength ratio	0.11
Input, output iris radii	3.15, 2.35 mm
Input, output iris thickness	1.67, 1.00 mm
Input, output group velocity	1.65, 0.83 % of c
First, last cell Q-factor	5536, 5738
First, last cell shunt impedance	81, 103 MΩ / m
Number of regular cells	26
Structure length including couplers	230 mm
Filling time	67 ns
Total pulse length	242 ns
Peak input power	61.3 MW
RF-to-beam efficiency	27.7 %
Maximum surface electric field	230 MV/m
Maximum pulsed surface heating	47 K

Table 2.1: Parameters of the structure

parts. Figure 2.5 shows a disk and a model of the accelerating structure. Figure 2.6 shows the actual test structure before installation.

The iris radius and thickness are linearly tapered in order to optimise the various high power parameters and to create a smooth field profile along the structure.

Because of the high number of bunches per train and of the very short spacing between them (see Table 1.1), the structure is designed to extract the transverse wakefields that can develop in the structure. This is realised using four symmetrical waveguides of dimensions carefully selected in order to allow the propagation of just the higher order electromagnetic modes (HOMs) but not the fundamental one that is used to accelerate the bunches and is provided from the input couplers. Once extracted, the transverse wakefields are damped on tips of Silicon Carbide (SiC) that are placed 50 mm away from the axis of the cavity. The tapering also provides detuning of the high order modes, which are an issue even for highly damped structures.

Cooling water circuits and the vacuum flange are also installed the structure. The "CC" in the cavity name refers in fact to the particular shape of the coupling cells of this structure.



(a) A disk composing the structure



(b) CAD model of the structure, open to show the damping material

Figure 2.5: A disk composing the structure (left) and the scheme of an accelerating structure (right), including couplers for the RF, cooling elements and connection flanges. The wakefield monitor is not present in the prototype under test.



Figure 2.6: The structure prototype after the brazing of the copper disks and before the installation (*Courtesy of A. Solodko*)

# Chapter 3

## The breakdown process

This chapter will present the detected physical effects of the breakdowns and some aspects of the related physics. Typical setups for studies of vacuum arc physics will not be presented indeed, and a good summary can be found in [25]. The particularity of the setup used in this work is the beam presence, that makes the majority of the sensors commonly used to study the physics of vacuum arcs blind or not installable. This work concentrates more on the effect of the beam presence on the breakdowns rather than on the vacuum arcs physics.

The large amount of parameters that play a role in the breakdown process makes research in this field very difficult. For the same reason it is also not straightforward to compare different experiments. This situation has led to a lack of consensus in the scientific community about the theoretical description of the phenomenon.

Researchers anyway converge on the fact that, in high vacuum condition, the vacuum arc initiation process is dependent by the surface and material properties, but is independent from the vacuum pressure itself [39].

Strong efforts in pursuing the understanding of the phenomenon have been made so far, resulting in the improvement of the maximum gradient achievable in accelerating structures and the development of the first simulation codes [40].

### 3.1 Detected effects of breakdowns in accelerating cavities

Most of the theories about breakdown converge on the fact that the breakdown and the field emission are different phenomena. While the field emission is always present, the breakdown of the field is a rare event, and depends by different causes, first of all the material.

Therefore in the detection of the breakdown a background current emitted by field emission is always present, but on top of that during the breakdown one can observe [41]:

- RF pulse reflection: after the breakdown the incoming power is reflected back
- An isotropical emission of X-rays. Unfortunately as these travel through the structure any information carried by the spectrum is lost
- Visible light emitted by the arc
- Current bursts exiting the cavity
- Vacuum level spikes: this effect fades with conditioning. As will be discussed in section 3.4

Other effects, such as shock waves, have also been observed [42].

Figure 3.1 shows an RF pulse and the current burst measured with the setup used in this work during a run without beam. The fall of the transmitted power and the raise of the reflected one are clearly visible. Comparing the area of the two signals to the previous pulse, it is clear that a significant amount of energy is missing. This is normally attributed to the large amount of energy necessary to sustain the plasma that forms during the breakdown. The current burst emitted by the cavity on the downstream beam position monitor (BPM) is visible qualitatively on the right. It has to be kept in mind that the BPM is placed far from the exit of the cavity, resulting in a poor charge detection because of the small solid angle covered. Also the proper device to collect the emitted charge would be a Faraday Cup, which cannot be installed in this setup because it would obstruct the beam pipe.

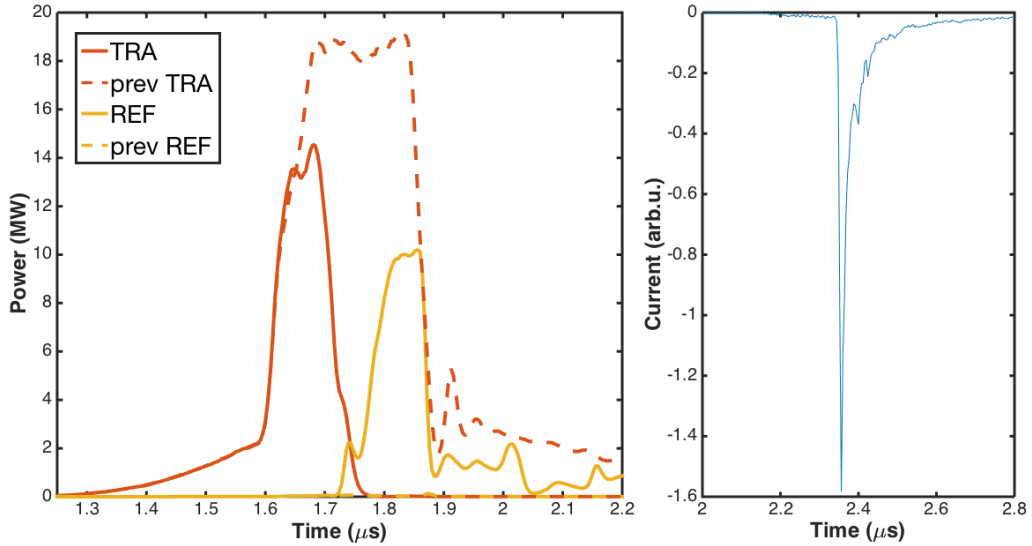


Figure 3.1: RF signals of a breakdown event (left) and burst of current emitted, detected by a BPM (right). The left plot shows the fall of the transmitted power (TRA) and the raise of the reflected power (REF). The RF signal of the previous pulse, without breakdown, is shown as a dashed line. Note that the time scale in the two plots are not the same.

## 3.2 Vacuum arc process description

A fully satisfactory theory to describe breakdowns has not been formulated yet, but the scientific community produced a number of models to describe the breakdown mechanism and initiation, summarised in [36, 43]. Most of them converge on the role that the field emission would have in triggering the breakdown, even if irrefutable evidences have to be shown yet.

### Triggers

The surface of the cathode is not completely flat, but presents some roughness that enhances the field emission as pointed out in chapter 2. This process leads to the formation of hot zones called *field emitters* where the local electric field is enhanced by a factor  $\beta$  because of the geometry and the current emitted is therefore increased (see Fig. 3.3, box a).

The current flow through the tip heats it up, modifying its physical properties and applying a tensile stress. Theories diverge on the process that takes place at this point: some are inclined to the heating up of the tip up to the fusion, like [35]; others on the cracking process of the tip due to the tensile stress applied by the enhanced electric field, which gets comparable to the tensile strength of the material around fields of 10 GV/m [40].

It is in any case possible that during this process the shape of the tip gets modified, enhancing the  $\beta$  factor even more.

### Plasma initiation

The peculiarity of the breakdown is that it takes place in vacuum, and has been detected even at large gaps. According to many experimental results, the plasma is created from the cathode material (regardless on how it got emitted from the surface). The cathode material forms a neutral gas surrounding the tip, that gets ionised by the electrons emitted by field emission (see Fig. 3.3, box b). In this first phase the ions created in this manner drift under the effect of the space-charge effect. The plasma initiation lasts only a few ns.

Spectroscopical measurements of the light emitted by the plasma have shown that the plasma is formed of ions with various charge, and electrons. The DC spark system at CERN showed that the plasma formed by copper cathodes present ionisation levels up to  $\text{Cu}^{3+}$  [25].

### Plasma evolution

The ion density of the plasma near the emitter results in the establishment of a sheath potential, which enhances the electrical field even more, provoking an exponential increase of the field-emitted current. The current emitted reaches values of several  $\text{A}/\mu\text{m}^2$ , resulting in the melting of the emitter (see Fig. 3.3, box c).

The molten metal becomes part of the plasma, that expands modifying temperature and density. The sheath potential gets modified as well. After an expansion process, where part of the plasma interacts with the surface, determining erosion, the greatest part of the ions recombine with the electrons determining an intense photon emission in the visible spectrum.

### Cratering phase

During the last plasma expansion, the ions impacting on the surface are expected to create new field emitters. The emitters will melt and result in an explosive emission because of the high field provoked by the sheath potential (see Fig. 3.3, box d).

The full arc is expected to continue up to the end of the RF pulse. Next, the plasma is expected to disappear due to expansion cooling or recombination. All the process results in a surface damage in the emitter zone and the surroundings. If in the damaged zone other protrusions have been created, they will trigger new breakdowns according to the new value of  $\beta$  (see Fig. 3.3, box e, f).

Figure 3.2 shows a photograph of a crater, taken using a scanning emission microscope.

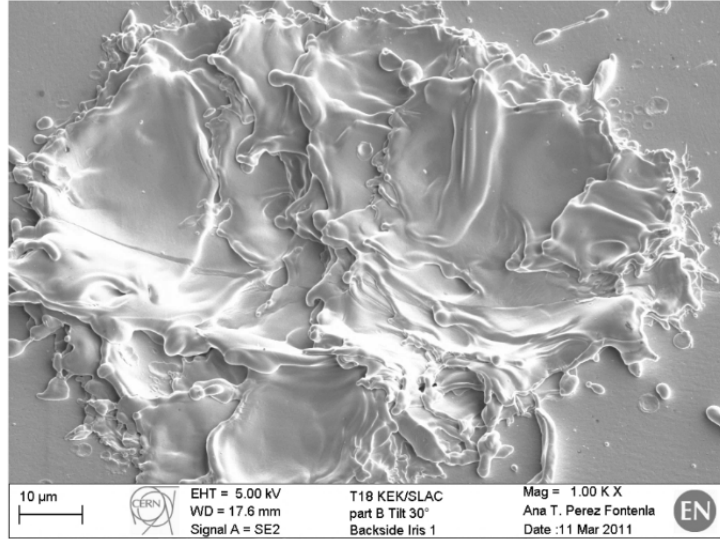


Figure 3.2: Crater provoked by a breakdown in an X-band RF accelerating cavity [30]

### 3.3 Breakdown rate scaling law

The interest on breakdowns in accelerator physics originate with the need to avoid as much as possible perturbations of the beam. The breakdown effect materialises mainly in kicks to the beam passing through the plasma [44], and



Figure 3.3: Breakdown stages in chronological order. From [25]

change of the acceleration because the reflection of the RF power modifies the field distribution inside the accelerating cavities.

A key parameter of an accelerating cavity is the breakdown rate (BDR). The breakdown rate is the number of breakdowns that happens per number of RF pulses. Measuring the BDR of a cavity implies measuring a probability, and requires to accumulate a sufficient number of pulses.

According to the latest developments, the BDR follows the scaling law

$$BDR \propto E_a^{30} \tau_p^5 \quad (3.1)$$

where  $E_a$  is the cavity accelerating gradient, and  $\tau_p$  the pulse length [30].

This scaling law allows one to compare the performance of different accelerating structures and different tests. It is important to underline that the scaling law was deduced by the results of the experiments executed so far, but does not contain any assumption on the physics of the breakdown process.

### 3.4 Influence of the conditioning process

It has been mentioned how the trigger mechanism of the breakdowns seems to depend on the condition of the surface of the accelerating cavity. In order to reach the low breakdown rate that is required for the performance of the linear colliders, two strategies have been used:

1. Refining of the production and assembly techniques of the cavities
2. Conditioning the structure with a series of RF pulses, increasing the power gradually and keeping the breakdown rate limited

The current production procedure for the structures for CLIC is outlined in [11]. The conditioning process is a more complicated matter.

The conditioning of an accelerating structure is achieved by repeatedly applying RF power pulses at a fixed pulse length, while keeping the breakdown rate limited under a certain threshold. This is realised by modifying the input power, that gets raised after a period without breakdown, or lowered if the breakdown rate gets too high. When the target power has been reached, the pulse length is increased, and the process restarts with low power pulses.

The process terminates when both the power and the pulse length target has been reached. In many experiments the breakdown rate has exhibited an exponential decrease with the conditioning time. The conditioning of a structure may last up to 3-4 months to reach the design breakdown rate. Understanding the process and finding the right conditioning strategy becomes important, and many efforts have been made in this sense. The most surprising result is that the conditioning process proceeds with the number of RF pulses rather than the number of breakdowns happened [45].

The physical process that provokes breakdown might change as long as the conditioning goes on. According to recent results [41], the vacuum level increase, that takes place during a breakdown, fades as time goes by. This effect is probably addressable to the stimulated desorption [36], that provokes a gradual release of the absorbed gas into the metal, that gets pumped out. This effect is triggered in presence of strong electric fields only, the same fields that are involved during the breakdown process. The contribution of the desorbed gas is still not clear anyway. Another possible effect is the presence of dust particles on the surface, that gets cleaned up as conditioning continues.

A review of the conditioning algorithm used, and the conditioning history of the accelerating cavity used in this work can be found in [46].

# Chapter 4

## Motivation of the experiment

The accelerating gradient profile in a travelling-wave cavity depends on the configuration of the electromagnetic field inside the cavity. The passage of the beam modifies the internal field configuration. As a consequence, the gradient profile is modified and decreases along the structure.

At the same input power, the modification of the gradient profile is dependent on the beam current, as shown in Fig. 4.1. The result of the beam loading of the cavity is a reduction of the average accelerating gradient.

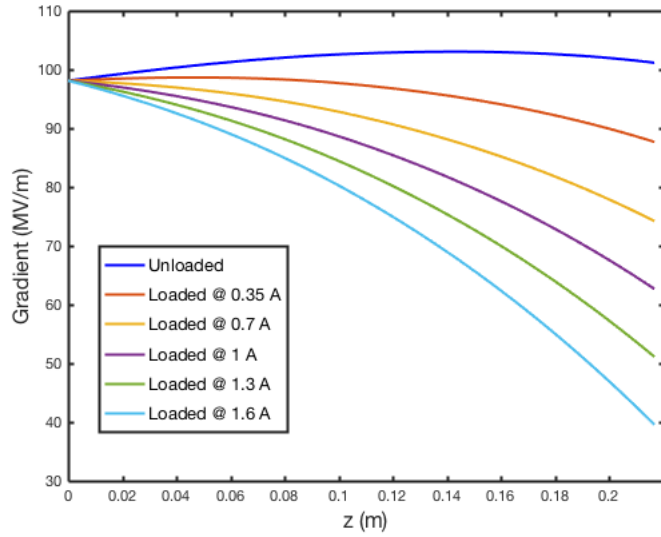


Figure 4.1: Gradient profile along the TD26CC structure at 43.3 MW input power. The unloaded case and the loaded with different current intensities are shown. The average gradient difference between the adjacent curves is approximately 5 MV/m.

The particle energy gain is given by

$$\Delta W = q \int_0^L E_{\text{acc}}(z) dz = q \langle E_{\text{acc}} \rangle L \quad (4.1)$$

where  $q$  is the charge,  $E_{\text{acc}}$  is the accelerating field and  $L$  the length of the accelerating structure.

Equation 4.1 shows that the energy gain is reduced when the accelerating cavity is loaded with the beam, compared to the unloaded condition. To compare the tests carried out without beam with the real running condition in an accelerator, it becomes necessary to raise the input power when the beam is present, in order to compensate for the reduction of average accelerating gradient. The nominal parameters for CLIC are 1.2 A of beam current and 100 MV/m of loaded accelerating gradient [11]. Figure 4.2 shows the variation of the gradient profile between loaded and unloaded running condition for the CLIC nominal operation. In this case the input power has to be raised from 43.3 MW to 61.3 MW to maintain the average accelerating gradient to 100 MV/m (see Table 2.1).



Figure 4.2: Comparison of the loaded and unloaded gradient profile of the TD26CC structure loaded with the CLIC Main Beam. When loaded with a current of 1.2 A, the input power to maintain an average gradient of 100 MV/m passes from 43.3 MW in the unloaded case to 61.3 MW in the loaded case.

All breakdown rate tests in literature have been conducted without beam presence. Since the vacuum arc phenomenon is not described yet by a solid physical theory there is no way to predict a priori how the breakdown rate is affected by the presence of the beam. The first dedicated experiment and its results are described in this work.

The interesting measurements that can be carried out are:

1. Comparing loaded and unloaded BDR at the same input power.
2. Comparing loaded and unloaded BDR at the same average gradient.

3. Studying a different field distribution inside the structure, by the effect of the antiloaded, i.e. the beam deceleration due to a different relative phase between beam and RF.

In the antiloaded condition, the field raises, as the beam releases energy in the cavity in the form of RF during the deceleration process. The comparison of the three running conditions is shown in figure 4.3.

In this work all the measurements outlined above have been performed. The results will be discussed in chapter 7.



Figure 4.3: Comparison of gradient profiles in different running conditions. The loaded and unloaded profiles are calculated at 43.3 MW input power, the antiloaded at 6.5 MW input power. The beam current in this case is 1.6 A.

# Chapter 5

## Experimental setup

The high-gradient tests at CERN are carried out in the three X-band<sup>1</sup> test stands (XBOXs). These are setups able to provide the necessary high-power RF pulses to the structures under test. For the tests described in this work the presence of the beam inside the accelerating cavity is also necessary, and is provided by the electron linac of the CTF3.

### 5.1 Linac and Dogleg

As mentioned in the first chapter, the main goal of the CTF3 is to demonstrate the feasibility of the CLIC acceleration scheme. For this reason, the linac is used to generate the Drive Beam pulse, that is sent to the rings for the recombination and then to the prototype Two-beam module.

The linac is realised using conventional 3 GHz technology. The recombination process leads to the bunch frequency of 12 GHz.

Given that the breakdown rate tests of high-gradient cavities was not in the initial design of the facility and differs from the standard operation, in the following sections only the part of the setup which is relevant for the breakdown experiments will be described. The full CTF3 accelerator complex is widely described elsewhere [11, 18, 47].

To perform high-gradient structure tests, a beam line parallel to the linac has been used. The two beam lines are connected by an oblique segment, resulting in the characteristic shape that is the origin of the name *Dogleg*.

For the high-gradient testing purpose the accelerator simulates the CLIC Main Beam. The parameters of the beam are reported in the Table 5.1

#### Injector

The production of the beam is realised by a 140-kV thermoionic gun, designed to deliver up to 5 A of current in nominal operation conditions. The gun is

---

<sup>1</sup>The X-band is a segment of the electromagnetic spectrum in the region of the microwaves. The waves in this region have frequencies between 8.0 and 12.0 GHz.

Current	1.6 A
Pulse length	250 ns
Energy	130 MeV
Reptition freq.	0.83 – 25 Hz

Table 5.1: Beam parameters used in the Dogleg [48]

followed by a S-band<sup>2</sup> prebuncher and a 17 cell travelling-wave buncher. These structures are followed by two 1.2-m long accelerating structures. The beam dimension in this initial phase is controlled by means of solenoids, up to the second accelerating structure [49].

Downstream of the injector a magnetic chicane with collimators is installed to eliminate off-energy particles and to perform bunch compression [50].

The layout of injector and chicane are reported in Fig. 5.1.

### Linac

Three modules composed of two S-band accelerating structures operating at 3 GHz are installed in the linac. The accelerating structures consist of 32 regular cells, operating in the  $2\pi/3$  mode. The damping of HOMs is guaranteed by radial slots in the iris, containing SiC loads. The structures are designed for fully loaded operation with a current of more than 4 A, but when simulating the Main Beam the current is significantly less, implying less loading. In this condition the energy gain is essentially bigger compared to Drive Beam operation.

The focusing is realised by triplets of quadrupoles, coupled with dipole correctors. The beam energy can be measured in the spectrometers in sector 4 and 10.

The layout of the linac is reported in Fig. 5.2.

### The dogleg

After sector 7 in the linac, another triplet of quadrupoles is located on the beamline, before a bending magnet. When the bending magnet is on, the beam is directed in the dogleg, passing through an oblique section, and is bent again to enter a segment of the beamline parallel to the linac. The optics of the dogleg beamline is designed to correct the dispersion provoked by the bending magnets. The structure under test is placed at the end of the dogleg line between two Beam Position Monitors (BPMs). Just before the structure there is a slit, in order to protect the coupling cell of the structure from being hit by a missteered beam. The beam is dumped downstream of the structure.

In case the first bending magnet is off, the beam proceeds straight in the linac, passing through a triplet of quadrupoles in section 9 and another triplet

---

<sup>2</sup>The S-band is the segment of the electromagnetic spectrum in the region of the microwaves. The waves in this region have frequencies between 2.0 and 4.0 GHz.

## CHAPTER 5. EXPERIMENTAL SETUP

---

in sector 10. A spectrometer is placed after that, to measure the beam energy.

The layout of the dogleg and of the linac up to section 10 is reported in Fig. 5.3.



Figure 5.1: Layout of the injector and the magnetic chicane. Legenda: SHBs: sub-harmonic bunchers.



Figure 5.2: Layout of the linac up to module 7. Legenda: bpm: beam position monitor.

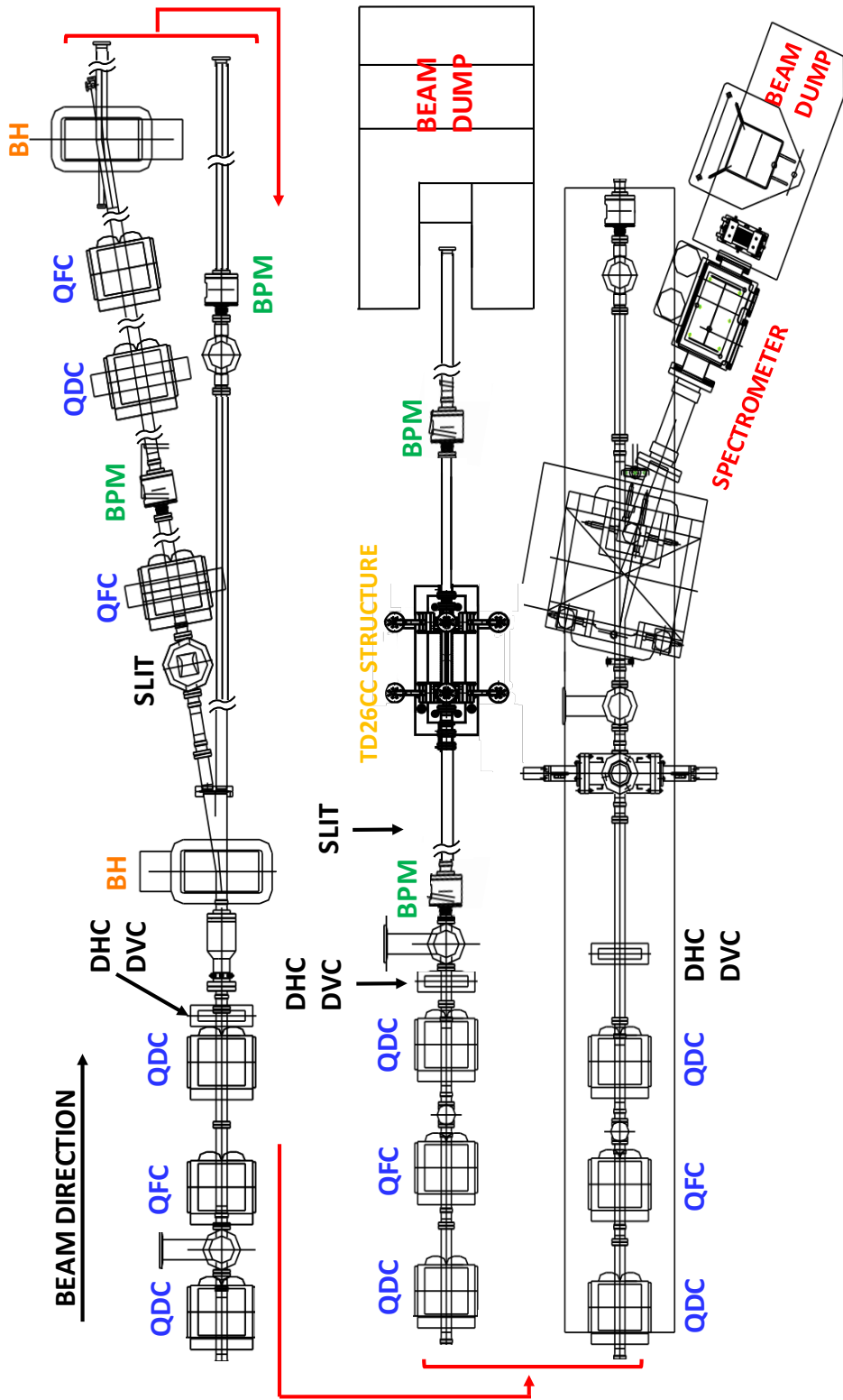


Figure 5.3: Simplified layout of optics and beam instrumentation of the dogleg line, adapted from technical drawings and facility layout [51]. The beam for this section come from the end of the module 7. Legenda: QFC(QDC): focusing(defocusing) quadrupole; DHC(DVC): horizontal(vertical) dipole corrector; BH: bending magnet in horizontal plane; BPM: beam position monitor

## 5.2 RF power production

The development of the accelerating cavity technology is strongly related to the possibility to produce and test prototypes. This test activity allows one to improve the understanding of the scaling laws of the phenomena that limit the performance of the accelerating structures, but also to compare the results of different production and conditioning techniques.

At CERN the production of 12 GHz RF was once carried out only in the Two-beam modules in the CTF3. To enlarge the test capabilities standalone test stands were necessary. This was realised for the first time with the installation of the so called X-Band Test Stand 1 (XBOX1) [52]. Similar test stands are present in the Nextef facility at KEK and in the ASTA facility at SLAC. Currently there are three X-band test stands simultaneously active at CERN.



Figure 5.4: Standalone X-band test stand layout

The layout of a RF test stand is shown in Fig. 5.4. It is normally formed by signal generation, amplification and delivery systems; diagnostic and control systems, and service systems such as cooling and protection systems.

### 5.2.1 The X-Box1 at CERN

The proposal of an X-band test stand at CERN followed the change of the frequency of CLIC from 30 GHz to the european X-band 12 GHz in 2008. An organic description of XBOX1 is in [53, 54]. The high-power RF production is realised using:

- an XL-5 klystron, able to produce 50 MW of 12 GHz radiation with a pulse length of  $1.5 \mu\text{s}$  and a repetition rate up to 50 Hz.
- a Scandinova modulator, used to power the klystron.
- a SLED-I type RF pulse compressor, able to compress the klystron output pulse to a shorter one of 140 MW, 250 ns long, which is sufficient to test accelerating structures considering the waveguide losses.

The RF delivery from the pulse compressor to the structure is realised using WR90 waveguides, kept under high-vacuum at a pressure of the order of

$5 \times 10^{-9}$  mbar. In order to reduce the losses, some part of the line to the structure under test is realised with low-loss waveguides. This structure requires mode converters because the fundamental modes of the waveguides are different. The overall transmission of the waveguide network has been measured to be around 67 %.

More details regarding the key components of the system are presented in the following sections. The system is controlled solely by the Low-Level Radio Frequency (LLRF), since the gain of the amplification chain is fixed. This feature requires a unique control system of the LLRF together with the Data Acquisition system (DAQ), that will be described in section 5.3.

### TWT, Klystron and modulator

The very first power amplification stage is carried out by a Travelling Wave Tube (TWT) [55], which is a device with the same working principle of the klystron (described below). It raises the power of the signal from some watts to up to 3 kW.

XL-5 klystrons comes from the effort made in SLAC to develop high efficiency klystrons for the Next Linear Collider project (NLC). They are based on the XL-4 klystrons, adapted from the american X-band frequency of 11.4 GHz to the european 12 GHz. This effort lead to the CPI VKX-8311A tubes that are currently in use [56], which are able to produce a pulse of 50 MW of power,  $1.5 \mu\text{s}$  long with an efficiency of the order of 40%.

Klystrons are vacuum tube amplifiers. They are composed of a thermoionic gun, that emits a pulsed beam of electrons. The beam passes through one or several cavities, where a low power RF modulates the beam. After a drift space, where the beam is kept collimated by a solenoid and accelerated by a fixed DC field, the beam passes through a passive cavity that extracts the high power RF. The beam is then dumped.

The klystron is operated in pulsed mode to reduce the wall-plug power consumption. This means that a power supply able to deliver short pulses of high power is necessary. XBOX1 uses a K-3 solid state modulator by Scandinova, able to supply voltage pulses up to 410 kV with currents of the order of 310 A.

### Pulse compressor

The pulse compressor is the device used to convert the long pulse of the klystron into a shorter one at a higher power. The operation principle is that the power from the klystron is stored in high-Q resonant cavities during the pulse. Before the end of the pulse the cavities are emptied by reverting the phase of the input power. The emptying process is done in a shorter time than the filling time, determining the production of a short high power pulse.

This technique can lead to peak power increase up to a factor 5-7.

The SLED-I type pulse compressor is using two cavities, coupled with a 3 dB hybrid coupler, in order to discharge the produced power to the desired

load instead of sending it back to the klystron. The theory behing the pulse compression is fully described in [57], the application in XBOX1 in [58].

The resonance frequency of the pulse compressor's cavities is strongly dependent on the volume, which depends on the temperature. For this reason the heat produced by the RF, due to the ohmic resistance of the walls, has to be disposed of by an external thermostatic system. An imperfect heat dissipation leads to the detuning of the cavities, which constitute an operational issue and will be extensively discussed later in section 5.5.2 and 6.1.3.

## 5.3 DAQ & RF control systems

The control system is in charge of generating a phase-modulated signal for the successive amplification stages (TWT and klystron). It also has to acquire the signals from the directional couplers, and the diagnostic signals from the structure and the vacuum systems. According to the diagnostic inputs, it modulates the signal and can also act on the beam permit of the gun of the linac. This last role is central, since the interlocking function is fundamental not only for the equipment protection, but also to trigger the data memorisation.

### 5.3.1 Hardware

To perform his task, the control system is made of different components, including PLCs (Programmable Logic Controller) interlock systems, VME (Vera Module Europa) crate based arbitrary signal generators, OASIS PC [59]-based digitisers and PXI (PCI eXtension Instrumentation)-based control systems.

The core of the system is the National Instrument PXI crate [60], that is the most advanced system in the setup. It carries out the acquisition and processing of all the signals relevant for interlocking the system; triggers the interlocks; save in the internal memory the recorded signals and retrieves the signals sampled externally in case of an interesting event; interfaces with the rest of the instrumentation.

Since the phase of the LLRF signal has to be modulated to be able to perform the pulse compression, the LLRF signal is sent to an analog and a digital phase shifter in series. During the experiments with beam, the digital one is used to properly phase the RF with respect to the beam.

The data acquisition from the -50 dB directional couplers on the waveguides is performed using different kind of sensors:

1. Diodes with a bandwidth of 500MHz convert the RF signals to a DC voltage level
2. IQ<sup>3</sup> demodulators are used to measure the phase and the amplitude

---

<sup>3</sup>In-phase and quadrature components demodulators. These detectors measure amplitude and phase of an electromagnetic wave by mixing it to a known wave at the same frequency (in this case supplied by the main 12 GHz oscillator of the Xbox).

3. Logarithmic detectors are used to acquire the signals with a wide dynamic range of over 46 dB

The PXI crate has 8 channels of 14-bits, 250 MSa/s digitisers. These digitisers are connected internally to FPGAs in order to perform the analysis as fast as possible, and send a signal to the trigger unit to interlock the LLRF signal production. A 24 channel Digital Multimeter (DMM) unit is used to read the vacuum signals from the ion pump controllers. The fast digitisers of the PXI acquire the signals from the logarithmic detectors.

The signals of the IQ demodulators are sampled by OASIS acquisition PC containing 16 units of 1 GSa/s, 8-bits ADCs. These are read by the PXI crate for the breakdown events and archived for the offline analysis.

The signals of the BPMs are acquired and recorded as well by one of the acquisition cards of the PXI crate.

Figure 5.5 shows schematically the high level RF described above and the acquisition equipment that is used for diagnostic and data analysis.



Figure 5.5: Schematic of the high level RF and the relevant part of the DAQ for the interlock system. See appendix for glossary of abbreviations

### 5.3.2 Online triggers

An interlocking system is implemented in the PXI crate, in order to detect the breakdown events and trigger the data saving. When one of the interlocks is triggered, it acts on the LLRF power, cutting the power but leaving the rest of the amplification chain ready. After a period of time, generally seconds, the power is restarted and ramped up gradually.

There are four interlocks of this kind, triggered when one of the following quantities exceeds a user-defined threshold:

1. Cavity peak reflected power:  $\max(P_{REF})$

- 
- |  |   |
|--|---|
| 2. Cavity reflected energy:              | $\int P_{REF}(t) dt$                      |
| 3. Cavity missing transmitted energy:    | $\int P_{INC}(t) dt - \int P_{TRA}(t) dt$ |
| 4. Peak power reflected to the klystron: | $\max(P_{KREF})$                          |

The last interlock is meant to protect the klystron, and is triggered when the reflected power back from the pulse compressor is too high. This happens especially when the pulse compressor is not properly tuned, as described later in this chapter. The first three indeed are used to detect a breakdown event inside the structure under test. When one or more of these four interlock is triggered, the event is saved by the PXI crate. In addition, an event is saved every minute, to monitor the state of the current test.

Generally a breakdown event triggers more than one of the criteria above. A key point is the redundancy: any of the interlocks triggers the event recording in order to not to lose any interesting event. Additional events that trigger the saving are stored anyway, and will be filtered out during the offline analysis described in the next chapter.

## 5.4 Other systems

### Cooling system

The operation of CLIC requires a component alignment on the  $\mu\text{m}$  scale. Once realised during the installation, the alignment has to be maintained keeping the thermal dilation under control. A number of studies have been carried out to this purpose, such as [61]. The thermal data from the accelerating structure installed in the dogleg are currently analysed as part of these studies.

The heating of the accelerating structures is provoked by the Joule heating induced by the RF encountering the resistive walls. In nominal conditions the heating is constant once the structure is running at constant RF input power.

In this perspective the breakdown events have a key role since they modify the heating, because of the perturbation of the RF power flow. This materialises both because of the power reflection by the plasma in the accelerating cavity, and the huge amount of power absorbed by the plasma, that can achieve the level of tens of MW.

### Vacuum system

In every accelerator an adequate vacuum has to be reached to preserve the quality of the beam. Compared to the traditional vacuum systems, in accelerators there are additional phenomena taking place. In fact, in addition to permeation, the desorption of surfaces is enhanced by beam losses and the photon emission from the beam.

An adequate pumping system is hence necessary, and is described in [47].

On top of the vacuum system for the beam pipes, the waveguide network has to be kept under high vacuum. Also in this case there is an additional

effect to the permeation, that is similar to the beam losses. The plasma that establishes during the breakdown process is formed by material evaporated from the cathode, and needs to be pumped out to restore the vacuum level as soon as possible. Furthermore, the vacuum arc emits electrons and ions that can enhance desorption.

## 5.5 Operation of the setup

One of the main tasks of the author of the thesis was to carry out the operation and supervision of the accelerator and of the 12 GHz RF production, in addition to the data analysis. It seems therefore appropriate to spend some words on the operation and the operational issues encountered in the CTF3.

### 5.5.1 Linac operation

During 2016 the CTF3 schedule foresaw running the Drive Beam during the week and switching to the Main Beam for the weekend. The reason is that the high-gradient testing experiments require a long beam time to collect data, because of the low breakdown rates. So they are carried out by leaving the accelerator running when it is not in use by other operators. A reliable system of interlocks is diagnosing the equipments and ensuring the protection of the accelerator.

As mentioned before, the linac of the CTF3 is normally operated in fully-loaded mode, producing a long high-current beam pulse of the Drive Beam. In order to produce the Main Beam for the BD tests, it is necessary to produce a short beam pulse with a lower current and a resulting higher energy.

The accelerating structures in the linac are powered by 45 MW klystrons equipped with pulse compressor system. The RF pulse shape is changed by modifying the phase program of the low level RF.

The current pulse duration from the gun is also adapted to the new beam. The beam optics was calculated to minimise the beam size in the accelerating structure, and the quadrupole gradients are set up accordingly.

This operation required normally slightly less than an hour, mainly due to temperature settling of the RF pulse compressors, sometimes up to a couple of hours.

The operation has to be supervised during the running, since the trip of some component can cause an interruption of the beam or of the RF production. The operation has been automatised to restart after the most common trips without operator intervention. Nevertheless, other faults have to be dealt with manually. The typical uptime without intervention is around one day.

### 5.5.2 Xbox operation

The repetition rate used is 25 or 50 Hz, to accumulate higher statistics.

## CHAPTER 5. EXPERIMENTAL SETUP

---

After a breakdown, the power is stopped as foreseen in the CLIC operational scenario. After the stop, the power is gradually ramped up. Overall, the power restoration lasts less than 10 s if no other breakdown happen.

Power dissipation changes leads to detuning of the pulse compressor. The detuning can be provoked by frequent breakdowns (which stops the RF production), switching from loaded to unloaded condition (normally because of problems on the linac; the RF input power level is lowered in some cases when there is no beam), or from the thermal day-night excursion. The pulse compressor detuning is accompanied by the increase of reflections to the klystron. A tuning algorithm has been implemented to face this effect. More details about the tuning will be given in section 6.1.3.

# Chapter 6

## Vacuum arc detection and localisation

### 6.1 Offline selection of the events

In order to perform the data analysis, a full analysis framework has been developed using MATLAB [62]. The selection of the interesting events will be described chronologically, as it is performed in the analysis program.

#### 6.1.1 Data collected from the PXI

As mentioned in the previous chapter, the data acquisition is performed from a real-time LabVIEW program running in the PXI crate. When an event fires at least one of the online triggers, it is saved into the crate's disk. Every 8 hours, the crate assembles a data file and stores it in TDMS format [63].

In order to proceed with the analysis, the files from a same day are merged in a new data file.

The kind of events that are collected by the PXI crate have two origins, and are flagged differently depending on whether they belong to:

1. Interlock pulses: an event that triggered at least one of the online interlocks. If available, the two precedent pulses are saved.
2. Regular pulses: the pulse data saved once per minute.

The first ones are sent to the next analysis step, the second ones are analysed separately to check the running condition of the accelerator and the RF systems.

#### 6.1.2 Power spikes detection

A key operational issue is the presence of power spikes, that sometimes are detected in the systems. If the spike causes an interlock to trigger, the event is recorded. An additional offline filtering layer is necessary to distinguish events containing a spike from the normal events.

The main characteristics of a spike are:

- Short duration: normally in the range 10-100 ns.
- Very high power burst: it can reach 60-70 MW or even more.

The first point makes the spikes easily detectable using a frequency filter to detect signals of such a short duration.

After careful investigation, the origin of the spikes has been addressed to the TWT. It has to be pointed out that the frequency of the spikes is anyway low compared to the rate of the breakdowns, and that after the first runs the replacement of a very active tube improved a lot the performance. As can be seen in Fig. 6.1, the spike can happen everywhere in the pulse.

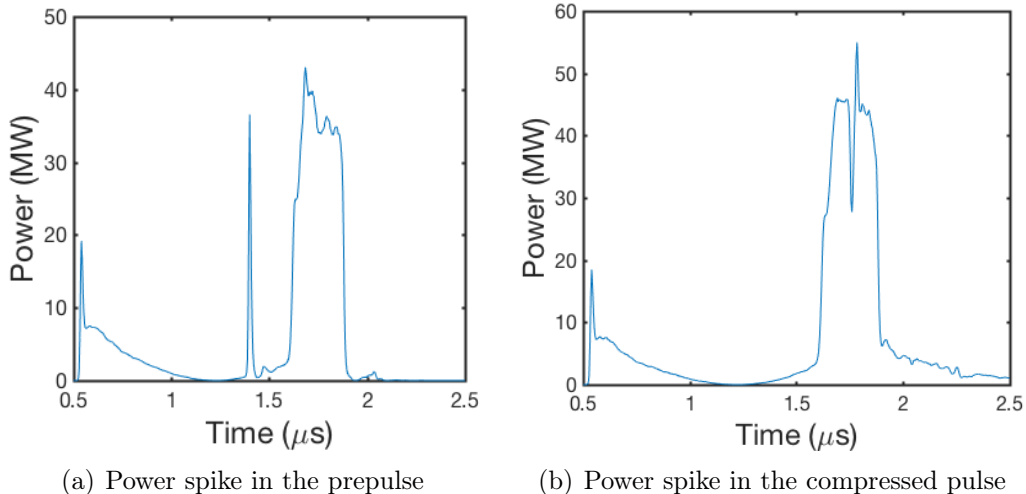


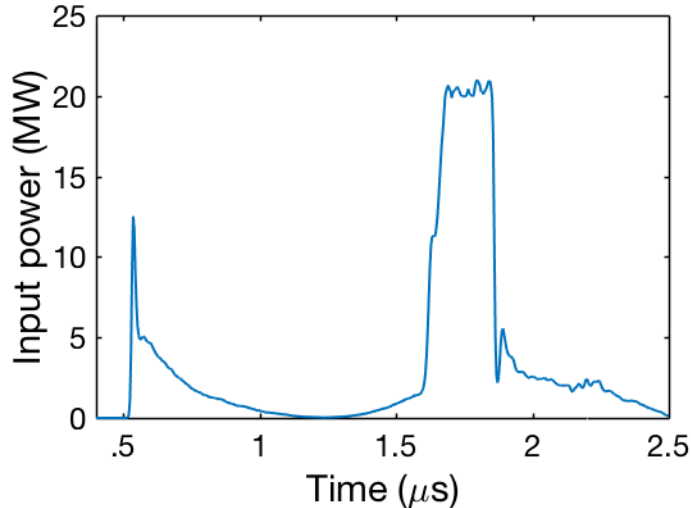
Figure 6.1: Cavity input power signal for two different spikes. Spikes can happen anytime in the signal evolution.

When a spike gets detected, the correspondent interlock is discarded, and also the following pulses for a given period of time (generally 90 s). It is believed that the burst of power brought from the spike may trigger strong breakdowns that damage the surface. This creates new emitters that trigger new breakdowns as long as the system does not reach an equilibrium. The waiting time before restarting to count the breakdowns gives time to the surface to get reconditioned.

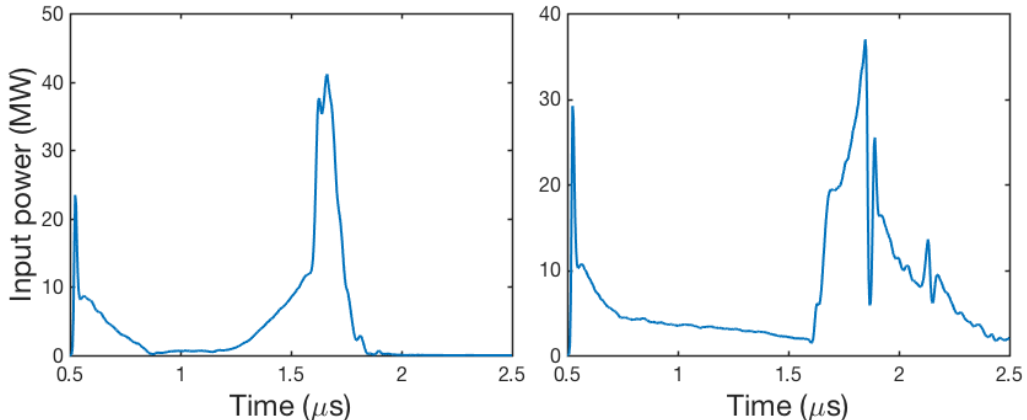
### 6.1.3 Pulse compressor tuning issues

RF tests of accelerating cavities are carried out using the CLIC nominal pulse, which is made of a filling (or rising) time of 70 ns and a flat-top 180 ns long (as shown in Fig. 6.2 (a)).

A common operational issue is the detuning of the pulse compressor, that provokes an imperfect shape of the RF pulse. This does not constitute an



(a) CLIC nominal RF pulse



(b) Undertuned pulse (right) and overtuned pulse (left)

Figure 6.2: The CLIC nominal pulse and two extreme cases of detuning of the pulse compressor.

issue for CLIC in the two-beam scheme without pulse compressors (unless implemented in the klystron option with pulse compressors).

The origin of the detuning is the difference of the total volume of the pulse compressor's cavities. This is controlled by changing the cooling water temperature, but as any other thermal system this needs time for the regulation [64]. The detuning is mostly an issue in summer, when the thermal excursion during the day is particularly high.

As a general rule, a slight detuned pulse is accepted as long as the detuning does not affect the pulse width. It has been calculated from the BDR scaling (Eq. 3.1) that the breakdown rate variation for a non-flat pulse with the same pulse width is 5%, taking into account that the peak power overshoot is limited to 10% by the control system [65].

During normal operation, the system oscillates between slight undertuning and the tuned condition. This can be ascribed to the implementation of the

tuning algorithm.

The data are discarded in case of extreme detuning such as in Fig. 6.2 (b) and (c), where the box-shape of the pulse is not recognisable anymore.

The slight detuning is not considered as a relevant source of error in the breakdown rate measurement, because of the short duration of the detuned periods with respect to the duration of the run and the little difference that would be induced in the breakdown rate.

#### 6.1.4 The metric

The RF diagnostic is based on the signals recorded by directional couplers of the incident power (INC), transmitted power (TRA) and reflected power (REF).

Since the accelerating structure is well matched with the rest of the RF system, the reflections are minimal. This means that during the normal operation only the INC and TRA signals are non-zero.

When a breakdown happens, the plasma in the structure acts as a short circuit [66], hence the RF incoming after the breakdown gets reflected back, and consequently the transmitted power falls.

The online selection of the events is chosen to be loose enough not to risk losing any interesting event. An additional filtering level is necessary to select the breakdowns happening in the structure. In order to filter the non-interesting breakdowns or fake interlocks two quantities are calculated:

$$m_{\text{REF}} = \frac{U_{\text{INC}} - U_{\text{REF}}}{U_{\text{INC}} + U_{\text{REF}}} \quad (6.1)$$

$$m_{\text{TRA}} = \frac{U_{\text{INC}} - U_{\text{TRA}}}{U_{\text{INC}} + U_{\text{TRA}}} \quad (6.2)$$

where the signal energy  $U$  has been evaluated from the power signal over the whole acquisition period  $T$

$$U = \int_0^T P(t) dt \quad (6.3)$$

For a non-breakdown event it will be  $m_{\text{REF}} \sim 1$  and  $m_{\text{TRA}} \sim 0$ , when the attenuation of the structure is taken into account.

Plotting the 2-D distribution of these two quantities, two distinct regions appear (see Fig. 6.3). The centre-left region is populated of the fake interlocks and the breakdowns that happen upstream the structure under test. The events happening in the structure are located in the lower right area on the plot.

The most common situations can be summarised as follows:

- Fake interlock, which is a normal pulse with no breakdown. In this case no energy gets reflected from the structure, consequently  $m_{\text{REF}} \sim 1$  and  $m_{\text{TRA}} \sim 0$ .

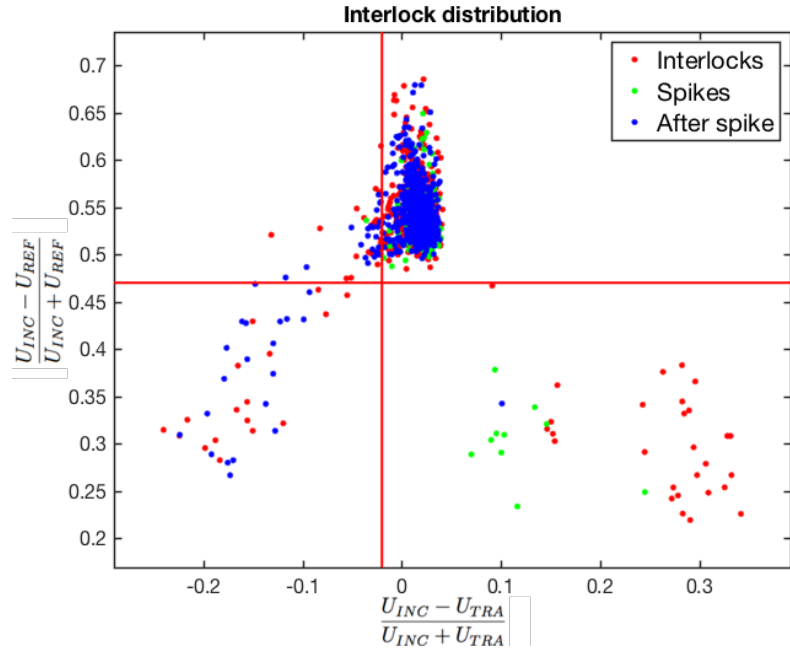


Figure 6.3: Metric plot for an unloaded run. Data grouped in two different regions are clearly visible. The lower-right region is containing the interesting interlocks, that are retained for the next analysis step. The thresholds are shown as red lines.

- Breakdown in the waveguide network, but before the input directional coupler. In this case the incident power pulse gets modified before reaching the structure, resulting in a lower  $U_{INC}$  (also  $U_{TRA}$  will follow the variation of  $U_{INC}$ ), but still there is no power reflected back. The metric will be again  $m_{REF} \sim 1$  and  $m_{TRA} \sim 0$ .
- Breakdown after the input directional coupler. In this case the RF signals will behave as outlined in section 3.1. This results in  $m_{REF} < 1$  and  $m_{TRA} > 0$ .

In this work the selection of the events has been performed using the two thresholds plotted in Fig. 6.3, but as future development more refined methods can be used, such as k-means clustering or neural networks [67].

### 6.1.5 Power back-off failure

According to the test procedure, after a breakdown the input power gets inhibited. Afterwards, the power is restarted and ramped up gradually to the nominal value unless a new breakdown happens. The duration of the stop and the ramp-up of the power takes generally less than 10 s and depends on the target-power level.

The reason for this behaviour is to preserve the surface of the accelerating cavity under test. The necessity of this procedure is foreseen to be verified by

testing a structure without backing off the power. No test of that kind has been done so far, and will be implemented in the future in one of the other test stands at CERN [68].

The data analysis showed that the power was not always cut immediately. This could trigger a breakdown following the original one, provoked by a malfunctioning of the instrumentation that did not cut the power. For this reason, all the events in the next three seconds have to be considered as an additional systematic source of error on the breakdown counting. More details on how the breakdown are counted will follow in section 6.3. This issue happens also in the other XBOX stands at CERN, and will be investigated in the future.

### 6.1.6 Additional criteria for runs with beam

During the experiments with beam, two additional conditions have to be met to consider an interlock as a breakdown with beam in the accelerating structure

1. The beam has to be present during the pulse.
2. In the case of a group of successive breakdowns, also called *cluster*, the initial breakdown has to be triggered during a pulse with beam.

## 6.2 Time and space positioning of the breakdowns

The detection of the breakdown position is based on the RF signals. The time taken by an incident signal to travel from the input directional coupler and come back after the reflection at the breakdown location is measured ( $\tau_{d,\text{REF}}$  in Fig. 6.4). The time for a signal to travel from the input to the output directional coupler is measured as well ( $\tau_{d,\text{TRA}}$  in Fig. 6.4). A full dissertation on various possible positioning methods is available in [42].

### 6.2.1 Edge method

The Edge Method is based on the difference between the arrival times of the falling edge of the TRA signal and the rising edge of the REF signal. This method constitutes the most reliable method used for breakdown positioning.

Assuming that the vacuum arc starts to absorb and reflect the RF immediately after being triggered, this method will identify the longitudinal position of the onset of the breakdown in the accelerating cavity.

The edges of the TRA and REF signals are identified by looking for the deviation point of the signal from the nominal pulse (see Fig. 6.5 (a) ). This is easily done using the previous pulse, which is recorded in the data when a breakdown happens. According to this method the time delay  $\tau_d^{\text{edge}}$  is

$$\tau_d^{\text{edge}} = \tau_{\text{REF}}^{\text{raise}} - (\tau_{\text{TRA}}^{\text{fall}} - \tau_{\text{FILL}}) \quad (6.4)$$

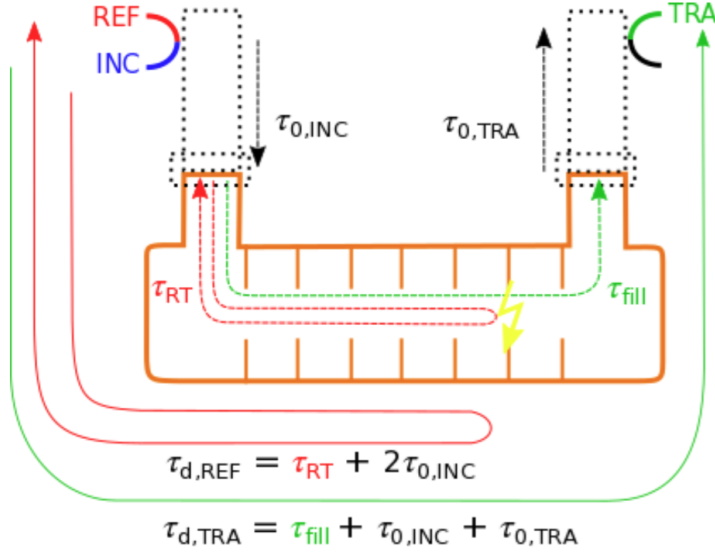


Figure 6.4: RF signal time delays in a travelling-wave accelerating structure. In the setup used for this experiment, the waveguide length for input and output couplers is identical and  $\tau_{0,INC} = \tau_{0,TRA}$

where  $\tau_{REF}^{\text{raise}}$  and  $\tau_{TRA}^{\text{fall}}$  are the time position in the signal of the deviation point from the previous pulse of the transmitted and reflected signals, and  $\tau_{\text{FILL}}$  is the filling time of the accelerating structure. This leads to a time delay that is included between zero and  $2\tau_{\text{FILL}}$ . No additional time delays have to be considered, since the cable lengths are the same.

For noisy signals, using the deviation point detection instead of detecting the edge of the signal at a certain height showed an improvement in the performance of the algorithm. In some cases, the previous pulse was not recorded, and the location of the signal edges was determined manually.

### 6.2.2 Correlation method

It has been outlined before that after the establishment of the breakdown, the incident power is reflected back. This means that looking at the tail of the signal after the compressed pulse it is possible to identify some particular pattern (see Fig. 6.5 (b)), and in a number of cases the same pattern will be visible in the REF signal returning back.

This method is not always successful since is strongly dependent on two factors: the amplitude of the pattern observed (in Fig. 6.5 (b) one of the best examples is reported, but most of the times the amplitude is much lower); and the position of the breakdown in the cavity, since a longer path of the signal in the structure leads to higher attenuation. In order to limit as much as possible the attenuation effect, this analysis is performed using the uncalibrated signals from the log detectors, but it is still not always possible to individuate a common pattern between the tails of INC and REF.

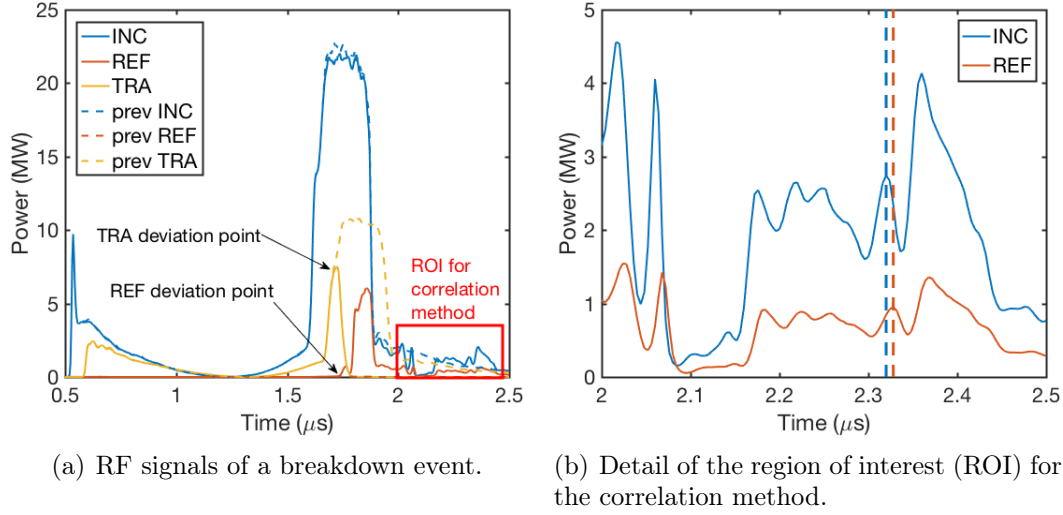


Figure 6.5: RF signals of a breakdown in the structure. (a) shows the RF signals for a breakdown event, where the deviation points of the TRA and REF signals are highlighted. The dashed lines are the reference signals, given by the previous pulse. (b) is a detail of the Region Of Interest (ROI) for the correlation method marked in red in (a). The time difference between the dashed vertical lines indicate the time delay between the pattern of the signals.

### 6.2.3 Comparison of the two methods

As just pointed out, the correlation method is not always successful because of the attenuation of the REF signal. In addition, comparing the results of the two methods, the distribution of the arcs in the cavity are definitely different. Figure 6.6 shows the difference between the breakdown distribution of the same dataset using the edge (left) and correlation method (right).

The distribution obtained using the correlation method presents a peak at the beginning of the structure, that is not obtained using the edge method. This overpopulation of breakdowns at the beginning of the structure has been observed in all the datasets processed for this work, but also in [42].

Figure 6.7 shows the comparison between the two different techniques. The solid line indicates the agreement of the two methods. It is clearly observable that the correlation method is more likely to yield estimates further upstream in the structure than the edge method, as outlined from the asymmetrical distribution.

An explanation for the asymmetry is given by the *breakdown migration* [53, 69, 70]. According to this hypothesis, if the breakdown onset position is found by the edge method and the position of the steady state stable breakdown is found by the correlation method, then Fig. 6.7 is consistent with the migration upstream in the structure.

The edge and correlation methods detect features of the data that are separated by  $\mathcal{O}(100 \text{ ns})$ , which is compatible with the migration hypothesis

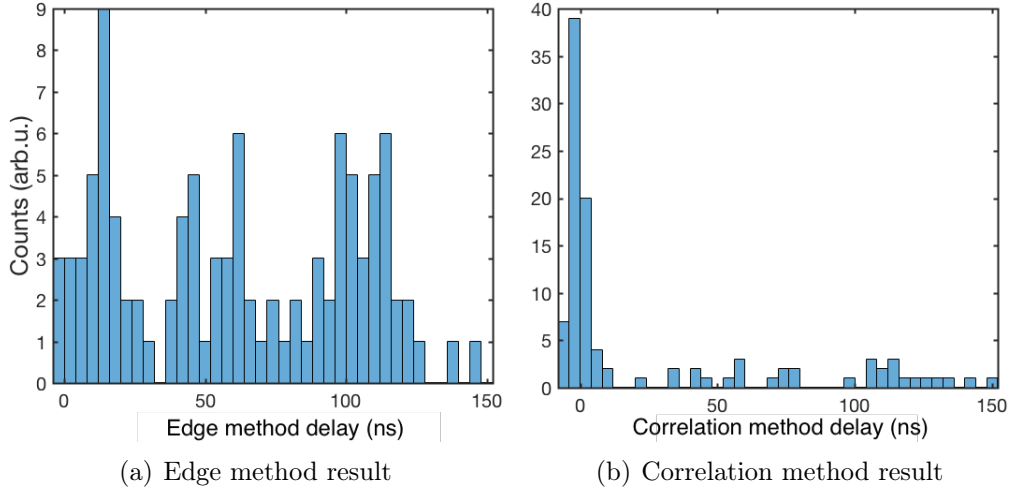


Figure 6.6: Comparison of the signal delay distribution for the edge and correlation method in an unloaded run. 75% of the events have been retained, in the other cases the correlation method was not applicable because of the attenuation. The spike in proximity of zero in the correlation delay is visible in all datasets.

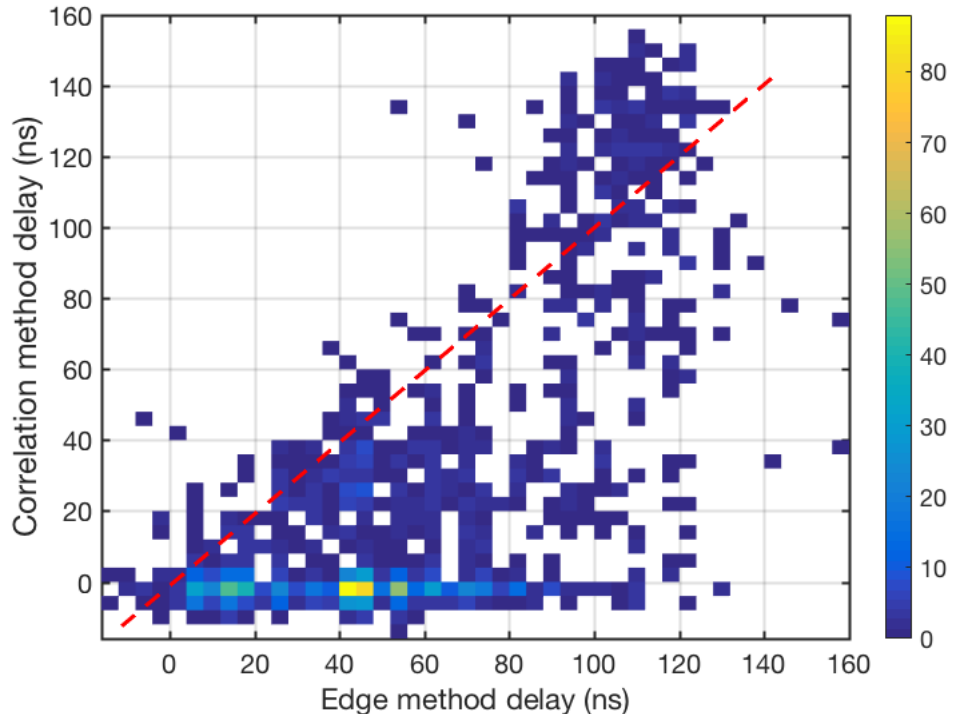


Figure 6.7: Comparison of edge and correlation method for the unloaded breakdowns. The straight red line represents the accordance of the two methods, the colors the number of counts per bin.

given that turn-on times of the arc of  $\mathcal{O}(10 \text{ ns})$  have been measured [71, 72].

A possible migration scenario is that the reflected power from the onset breakdown resonates with the incident power, enhancing the field in upstream cells. At this point a new breakdown happens upstream and the initial arc gets extinguished because it does not receive further incident power anymore.

Downstream migration is not likely, as little or no power is remaining downstream after the arc starts to reflect the incident power.

A possible migration scenario is presented in Fig. 6.8. The authors of [70] propose that the arc absorbs, but does not reflect incident power temporarily while migrating. The absorption causes a dip in reflection, right before the arc re-establishes itself at a new location.

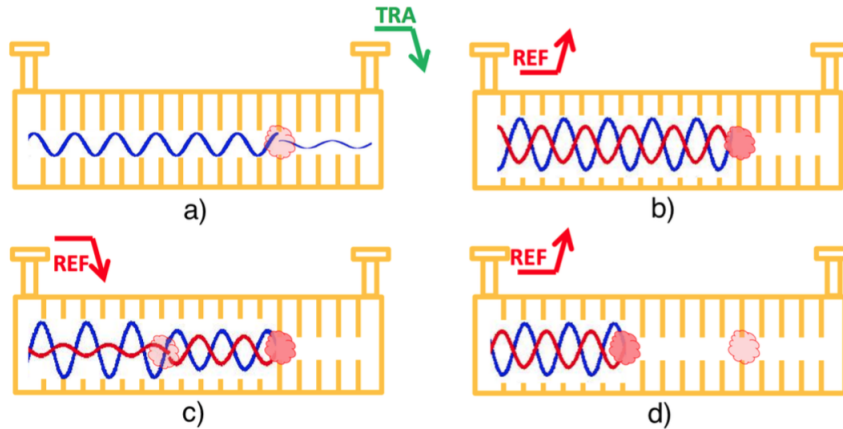


Figure 6.8: A possible migration scenario [70]: a) A breakdown establishes in the structure, absorbing the incident RF; b) The established arc reflects the incident RF; c) Constructive interference between reflected and incident RF provokes another arc upstream; d) As the second arc is established, any remaining power downstream is drained and the first arc gets extinguished

Figure 6.9 and 6.10 show the comparison of the positioning methods in the antiloaded and loaded beam configurations.

In the antiloaded case the majority of the breakdowns are happening at the end of the structure. No evidence of migration towards the beginning of the structure is present. This can be ascribed to the limited input power (6.5 MW) and the fields profile along the structure, that follows the gradient profile in Fig. 4.3. As a result, the field superposition of the incident and reflected RF is not sufficiently high to trigger any upstream breakdown, resulting in a short or absent migration.

In the loaded case, the majority of the breakdowns are migrating to the beginning of the structure. In this case most of the breakdowns are triggered in the first part of the structure, and the field has a maximum in the first cell, since the incident RF fields get reduced along the structure by the beam-loading. These two factors might justify the behaviour in Fig. 6.10, as the maximum of the superimposed incident and reflected RF should be at the beginning of the structure.

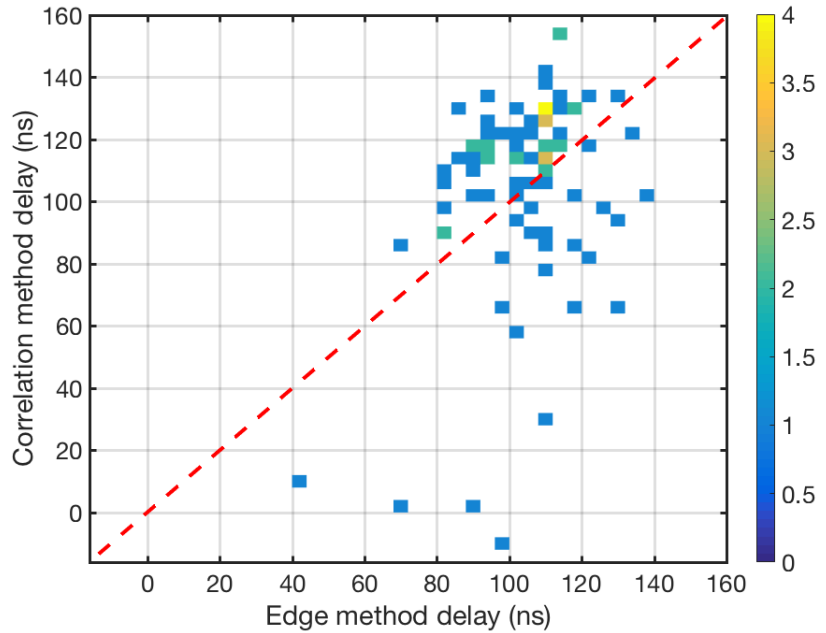


Figure 6.9: Comparison of edge and correlation method for breakdowns in the antiloaded case. The straight red line represents the accordance of the two methods, the colors the number of counts per bin.

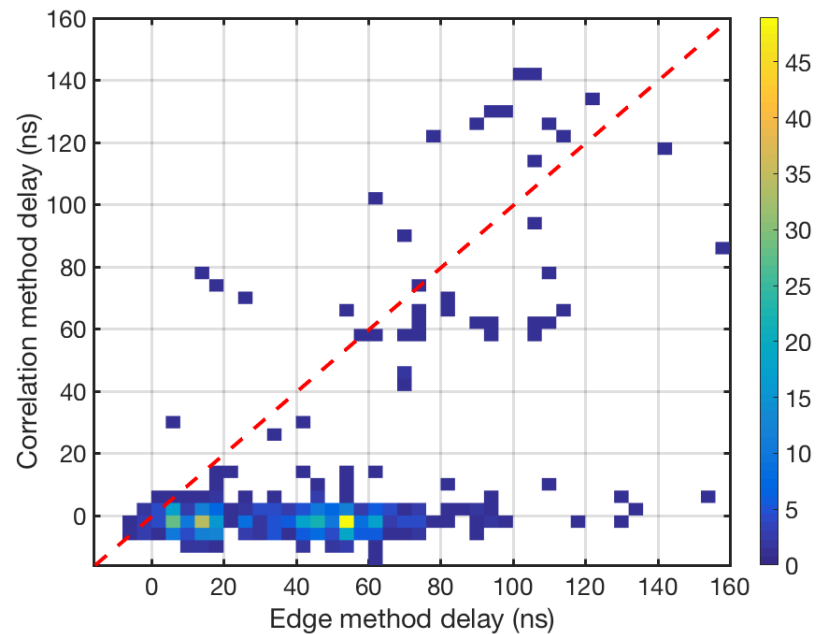


Figure 6.10: Comparison of edge and correlation method for breakdowns in the loaded case. The straight red line represents the accordance of the two methods, the colors the number of counts per bin.

Considering the effects highlighted above, only the edge method will be used for the following development of this work.

#### 6.2.4 Time to space conversion

In principle, the analysis of spatial position or temporal delay of the signals is expected to lead to equivalent results. However for a matter of convenience, it is better to refer to the cell where the breakdown has happened. For this purpose, it is necessary to convert the time delay in longitudinal position and then distribute the breakdowns in the corresponding cells. The time-space conversion is carried out considering that the round-trip time  $\tau_{RT}$  of the reflecting signal is given by (see Fig. 6.11)

$$\tau_{RT} = 2 \int_0^{z_{BD}} \frac{1}{v_g(z)} dz \quad (6.5)$$

where  $z_{BD}$  is the spatial position of the breakdown in the structure and  $v_g$  is the group velocity.

Equation 6.5 has been used to build a look-up table, that once inverted is used to determine the longitudinal position of the breakdown given the time delay, and hence the corresponding cell.

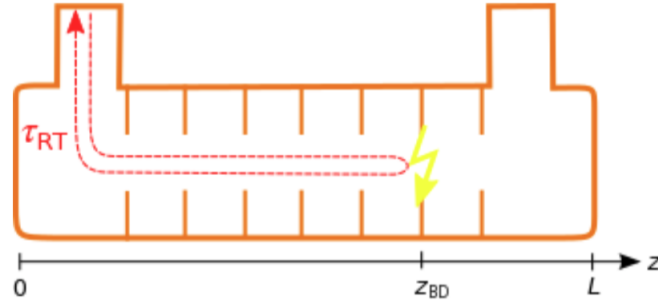


Figure 6.11: REF signal path in the accelerating cavity

### 6.3 Final data selection

The final goal of the data selection is to provide the number of breakdowns per run, that will be used to calculate the breakdown rate.

Ultimately, the data selection process that has been described is able to sort out all the fake interlocks and the breakdowns that are happening in the waveguide network or out of the desired experimental conditions. The product of such a selection is a group of interesting events that can have taken place in three different regions:

1. Between the input directional coupler and the input coupling cell (included).

2. In the regular cells of the accelerating structure.
3. In the output coupling cell (included) and the waveguide to the RF load.

Strictly speaking, only the breakdowns happening in the regular cells and in the coupling cells should be considered in the breakdown rate calculation. Here, the breakdowns in the waveguides connecting the directional couplers to the coupling cells are included, as it is extremely difficult to distinguish in which region the breakdown happened. The reason is that the group velocity in the regular cell is  $\mathcal{O}(0.01 c)$  and in the waveguides is  $\mathcal{O}(c)$ . In addition to this, the propagation time of the RF from the directional coupler to the coupling cell is of the order of 4.8 ns (from numerical simulations), which is extremely close of the sampling time of 4 ns used in the log detectors.

If a breakdown happens in these waveguides, it would lead to an overestimation of the breakdown rate. For this kind of experiment, an overestimation of the breakdown rate is acceptable, but an underestimation of the breakdown rate is not tolerable. The reason is that an overestimation of the breakdown rate in the tests would lead to a superior performance in CLIC once built, while the opposite is not desirable.

In the view of the above considerations, the number of breakdowns and its error are calculated as follows:

$$n_{BD} \pm \sigma_{\text{Poisson}} \pm \sigma_{\text{Back-off}} \quad (6.6)$$

where  $n_{BD}$  is the number of breakdowns,  $\sigma_{\text{Poisson}}$  is the statistical error on the number of breakdowns and  $\sigma_{\text{Back-off}}$  a systematic error coming from the malfunction of the system that misses to back-off the power after a breakdown.

The components of Eq. 6.6 are expressed according to the following considerations:

- the number of breakdowns  $n_{BD}$  is the number of breakdowns that are within the metric thresholds.
- the poissonian error  $\sigma_{\text{Poisson}}$  is used since the breakdown events are rare, and it is therefore reasonable to assume that this phenomenon follows the Poisson distribution.
- the missed back-off error contribution  $\sigma_{\text{Back-off}}$  is given from the malfunction of the Xbox. The error is estimated as the number of secondary breakdowns that happen in the next three seconds from an initial one.

$$\sigma_{\text{Back-off}} = {}^{+0}_{-n_{BDs \text{ follow-ups}}} \quad (6.7)$$

It has to be noted that calculating the number of breakdowns  $n_{BD}$  the number of secondaries happening in the following three seconds has not been subtracted. This is done to not underestimate the breakdown rate. This effect is taken into account adding the last error contribution.

The breakdown rate is finally calculated as

$$BDR = \frac{n_{BD}}{n_{\text{pulses}}} \quad (6.8)$$

where  $n_{\text{pulses}}$  is the number of pulses and is assumed to be without error. This is a reasonable assumption since the error on the pulse counting is in the worst case scenario a few hundreds of pulses, while measurements involve several millions of pulses.

# Chapter 7

## Results and future developments

### 7.1 Measurement summary

#### 7.1.1 Input power levels

A number of measurements have been collected during 2016. Figure 7.1 shows the relation between the average gradient and the input power in the accelerating structure with the measurement points highlighted. The measurement points have been selected to allow the comparison between the different running conditions, as outlined in chapter 4, and are summarised in Table 7.1.

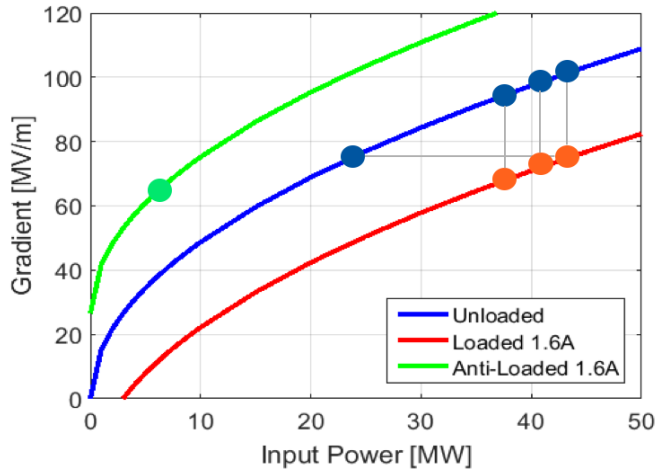


Figure 7.1: Average gradient as function of the input power in different running conditions. See text for details on the measurement points.

The measurements at different input power level have not been taken in a precise order, though it has been tried to keep long measurement periods as much as possible at the same input power. The choice was complicated by the fact that the Xbox was not able to provide the maximum RF power level during the year, mainly because of operational issues.

Run type	Input power (MW)
unloaded	43.3, 41, 38 and 24.6
loaded	43.3, 41 and 38
anti-loaded	6.5

Table 7.1: Input power levels of measurements of 2016 measurement campaign.

### Comparison of loaded and unloaded runs at same average gradient

For the CLIC test purpose, carrying out a measurement at 100 MV/m average gradient comparing loaded and unloaded runs would be the most interesting measurement possible. In order to perform it, the input power has to be raised from 43.3 MW in the unloaded case to 61.3 MW in the loaded case.

Unfortunately, it was clear from the beginning that reaching 61.3 MW of input power was not possible because the waveguides that deliver the power from the pulse compressor to the structure under test had excessive breakdowns for such high power flux.

Because of this limitation, the choice was limited to perform measurements at the same input power and compare the results or back off to much lower input power.

During a period of technical problems, data has been collected for an unloaded measurement at 24.6 MW of input power, which results in 76 MV/m average accelerating gradient. These can be compared with the the loaded case when running at 43.3 MW of input power, corresponding to an average gradient of 72 MV/m.

Unfortunately, with a such low input power, the breakdown rate is very low, and after 4 days of measurements zero breakdowns were collected. Therefore it is only possible to calculate a limit to breakdown rate in this running conditions. Table 7.2 shows the results of the compared running conditions

Run type	Peak(average) gradient	BDR ( $10^{-5}$ BD pulse $^{-1}$ )
Unloaded @24.6 MW	77 (76) MV/m	$< (7.7 \pm 7.7) 10^{-3}$
Loaded @43.3 MW	98 (72) MV/m	max. $2.8^{+0.2}_{-0.5}$ min. $0.3 \pm 0.09$

Table 7.2: Gradient parameters and measured breakdown rates for runs at 75 MV/m average accelerating gradient. In the last measured BDR, the error result symmetric because no missed back-off pulse was registered.

The results in Table 7.2 shows a higher breakdown rate in the loaded case, where the average gradient is lower, compared to the unloaded case. This consideration allow to conclude that the breakdown rate is not ruled by the average gradient.

Using the peak accelerating gradient instead of the average one, it is possible to calculate the ratio of the breakdown rated by means of Eq. 3.1. The

expected ratio between the unloaded and the loaded BDR is  $0.8 \cdot 10^{-3}$ , which is compatible with the data collected.

In order to reproduce the CLIC operational conditions, it is necessary to repeat the experiment in a setup able to support the high power involved, at an average gradient of 100 MV/m.

### **Comparison of loaded and unloaded conditions at same input power**

Aside the measurement presented above, it was not possible to compare loaded and unloaded runs at the same average gradient because of the wide difference in input power required. The measurements carried out during the 2016 campaign focused on comparing run with and without beam at the same input power. The input power levels used were 43.3, 41 and 38 MW.

### **Study of the antiloaded runs**

The antiloaded measurements were carried out at 6.5 MW of input power. With this input power and a beam current of 1.6 A, the field at the downstream end of the structure reaches the level of the maximum field of the unloaded tests (see Fig. 4.3). The results were indeed interesting and will be shown later in the section about the breakdown distribution.

#### **7.1.2 Beam pulse parameters**

As mentioned in the motivation of the experiment, the goal is to understand the effect of the beam on the breakdown rate. The beam parameters have been therefore selected in order to enhance the effect of the beam, rather than try to simulate the CLIC operation.

This materialises in:

- Higher beam current than CLIC: 1.6 A instead of 1.2 A.
- Longer beam pulse: the beam is lasting for 250 ns during all the compressed RF pulse, instead of last just during the flat-top of the CLIC pulse (see section 6.1.3). This avoids exceeding the flat-top loaded power level.

The loaded operation is clearly visible in the RF signals, as shown in Fig. 7.2.

## **7.2 Breakdown rate measurement results**

The breakdown rate has been calculated per every run, as described in section 6.3 and is reported in Fig. 7.3.

A fluctuation of the breakdown rate is appreciable. Considering separately unloaded or loaded runs data at the same input power, the excursion of the fluctuations is estimable as one order of magnitude.

## CHAPTER 7. RESULTS AND FUTURE DEVELOPMENTS

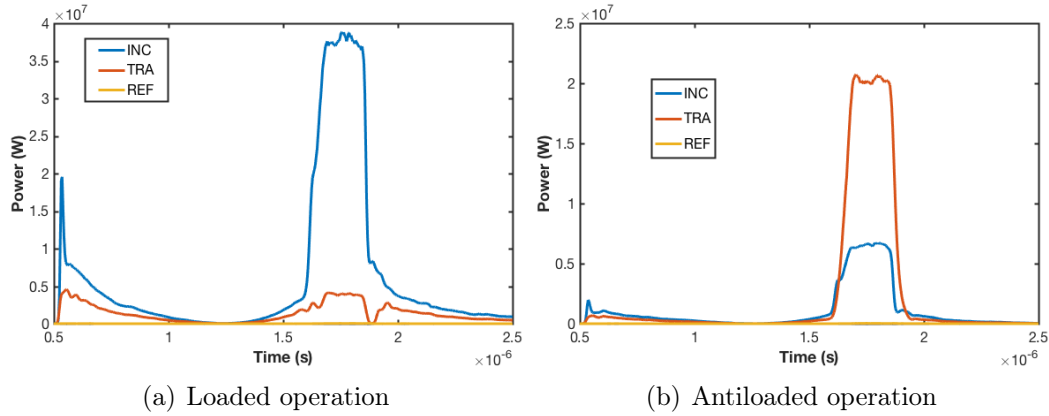


Figure 7.2: Comparison of the RF signals during the loaded and antiloaded operation. During the loaded operation it can be observed that the transmitted power falls close to zero, because of the energy transferred to the beam. The opposite behaviour can be noted in the antiloaded case, where the input power is much lower than the transmitted. In this case the difference in energy is provided by the beam, that gets slowed down because of the decelerating phase of the RF.

An unexpected behaviour is observed from July on, when the BDR raises for more than two months long, while running at 38 MW input power. It is possible that the antiloaded runs between June and July (plotted in green) have some effect on the overall BDR of the following runs. A similar variation of the breakdown rate is observable when changing the input power level of the structure.

In general, breakdown rate measurements need stable running conditions, and a fluctuation of the BDR is appreciable also in the unloaded tests in the other Xboxes. Normal measuring times involve measuring periods of the order of weeks. In this experiment, the average stable running time was alternatively four days without beam and 2 days running with the beam (up to two half-days per week are normally lost in operation and down-time). It is not possible to estimate the impact of this on the breakdown rate. Considering that when changing the input power, the BDR seems to increase, it is reasonable assume that the accelerating cavity is a system that needs a settling time to stabilise. A similar process could take place when switching form operation with beam to without and vice versa. The reason is that even if the input power remains the same, the fields inside gets modified and the structure needs time to settle.

A new insight on the effect of the input power variation will be given in the near future from the DC test stand at CERN, that has the possibility to acquire data much faster than any other RF-based experiment [68].

To investigate these effects in the same conditions, it is necessary to repeat the experiment with longer run times. This requires several weeks of dedicated beam time for the loaded runs, that the CTF3 was not able to provide because of the wide experimental program.

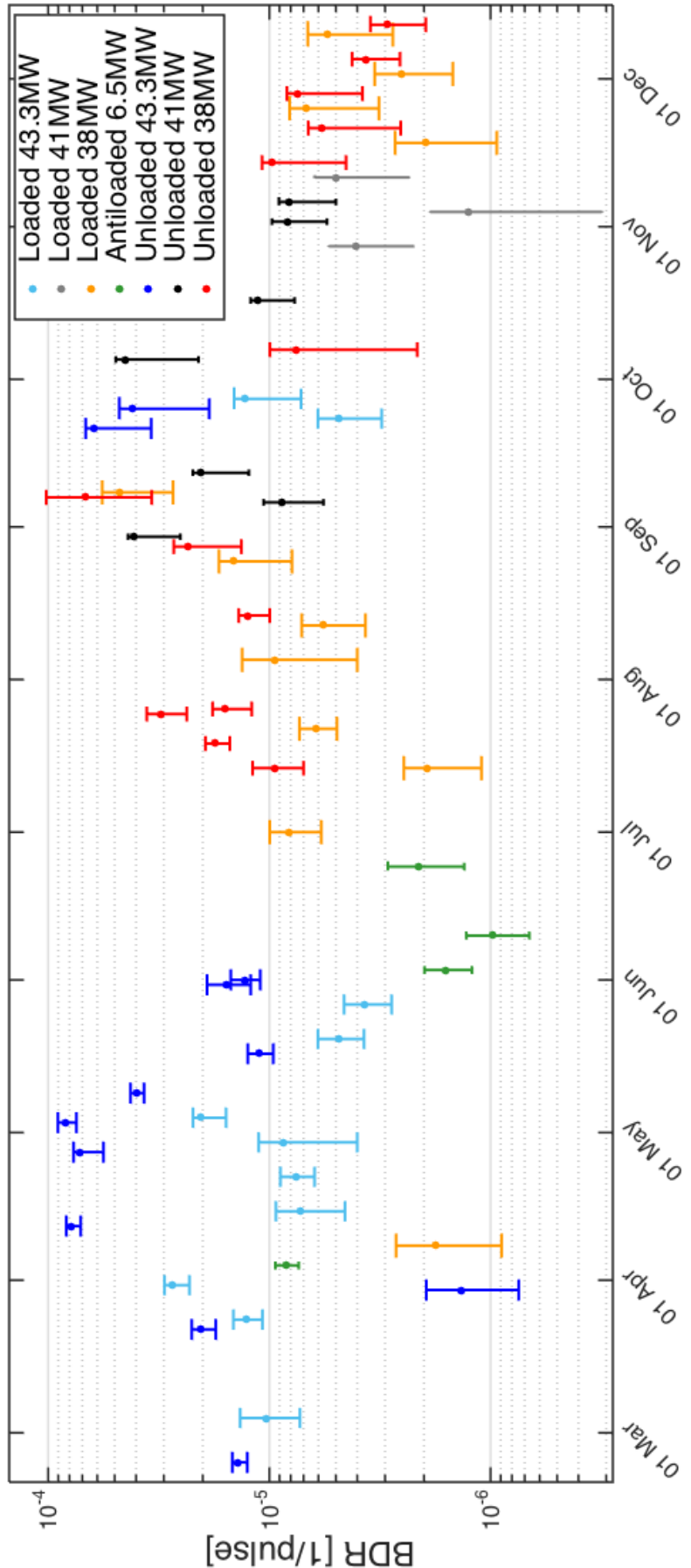


Figure 7.3: History plot of the measured breakdown rate for various measurement conditions.

It is possible anyway to observe the variation of breakdown rate at the same input power in some stable running periods. Figure 7.4 shows the detail of three running period at constant input power. Data show that running at the same input power, the breakdown rate is up to an order of magnitude lower.

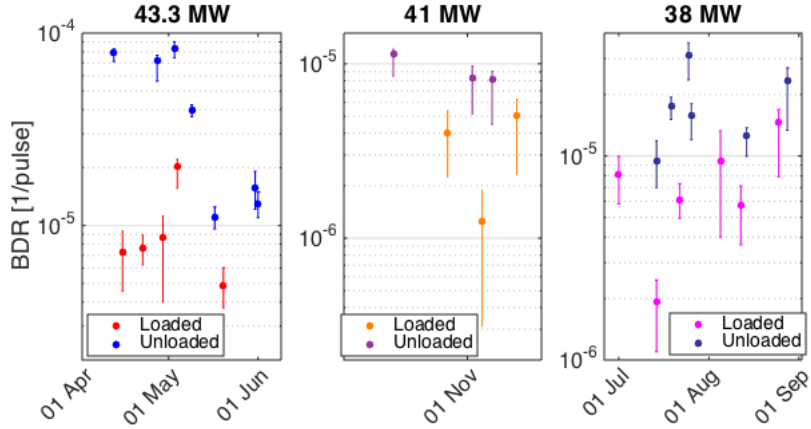


Figure 7.4: Comparison of the breakdown rate at different input power in three periods of stable running without altering input power.

This behaviour can be ascribed to the different field profile in the loaded and unloaded case. In fact, the peak gradient is 5% lower in the loaded case compared to the unloaded. According to the scaling law in Eq. 3.1, this difference induce a breakdown rate 3.87 times higher in the unloaded case. Taking into account this factor, the BDR in the loaded and unloaded cases oscillates around the same values. The parameters sustaining this reasoning are reported in Table 7.3. These considerations show the data in Fig. 7.4 under a new light: the beam presence itself is not reducing the breakdown rate, but induce a reduction of the BDR because causes the modification of the internal field profile.

Input power	$E_{\text{peak}}^{\text{unloaded}}$ (MV/m)	$E_{\text{peak}}^{\text{loaded}}$ (MV/m)	$(E_{\text{peak}}^{\text{unloaded}}/E_{\text{peak}}^{\text{loaded}})^{30}$
43.3 MW	102.6	98.1	3.87
41 MW	99.9	95.5	3.87
38 MW	96.1	91.9	3.87

Table 7.3: Gradient parameters for runs with and without beam at the same input power.  $E_{\text{peak}}$  is the peak accelerating gradient.

It has to be noted that there are two exceptions to the last affirmation: the unloaded run at 43.3MW input power at the end of March (plotted in blue in Fig. 7.3), and the last loaded run of the year at 38 MW input power (see dedicated plot in Fig. 7.5).

In the first case, it is not clear why the BDR was that low, even it looks an anomaly considering the general trend of the precedent runs. It also has to

be pointed out that the run is shorter than the others.

Regarding the second case, the BDR of the loaded and unloaded runs seems to converge at the end of the year. In addition, the last loaded run present a higher BDR than the precedent and following unloaded runs. Most likely this behaviour is addressable to a statistical fluctuation, but it is impossible to verify the further evolution because of the stop of the experiments at the end of the year.

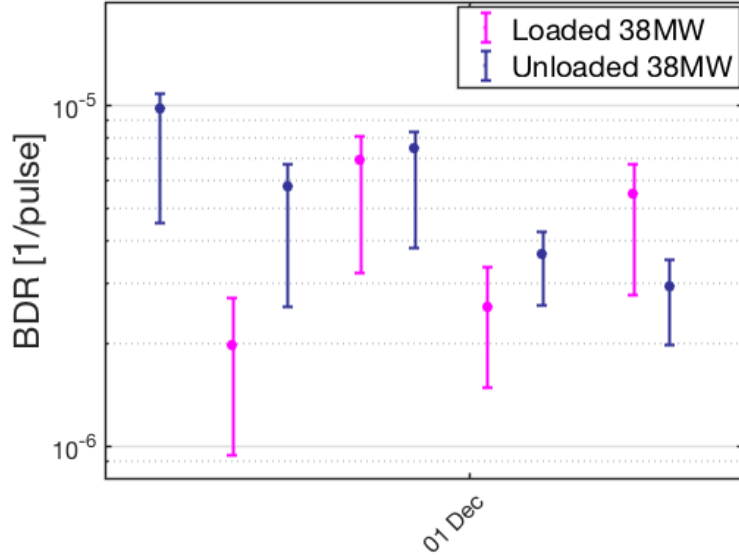


Figure 7.5: Measured breakdown rate at the end of the year

## 7.3 Breakdown distribution

### 7.3.1 A model for the breakdown distribution

Unloaded experiments exhibit a flat distribution of the breakdowns in the accelerating structure. In addition, it is known that the overall structure breakdown rate follows the scaling law in Eq. 3.1, but it has been derived from the data available from unloaded tests as well. From these considerations arises the necessity to understand if these results are still valid when running with the beam inside the accelerating cavity.

Considering any cell as a substructure, it is reasonable to suppose that cells with a higher accelerating field will be more likely to experience breakdowns than cells with a lower field. According to this reasoning and following the Eq. 3.1, the breakdown probability per cell is given by

$$\text{BD probability} = \frac{\left(\frac{E_{\text{cell}}}{E_{\max}}\right)^{30}}{\sum \left(\frac{E_{\text{cell}}}{E_{\max}}\right)^{30}} \quad (7.1)$$

where  $E_{\text{cell}}$  is the maximum surface electric field of the cell and  $E_{\max}$  is the maximum surface electric field of all the cells.

The choice of using the surface electric field instead of the accelerating gradient comes from the physics of the breakdown process [68]. Anyway the shape of the gradient profile and of the surface electric field along the structure differ only slightly. The field of the coupling cells is assumed to be identical to the adjacent cells. This comes from geometrical considerations, and could be eventually derived from simulations [73].

The result is shown in Fig. 7.6. The expectation is to have a flatter distribution compared to the others in the unloaded case, with an accumulation of the number of breakdowns in the first part of the structure for the loaded case and at the end of the structure for the antiloaded case.

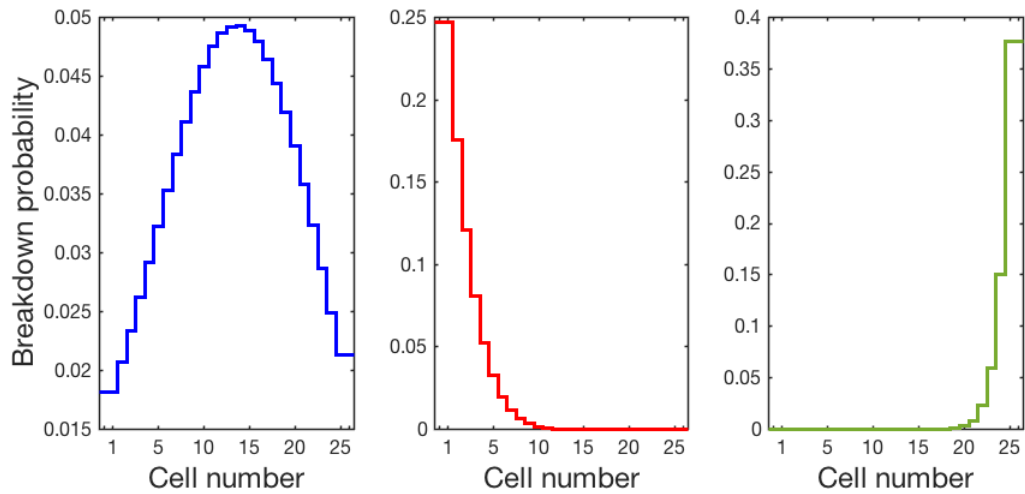


Figure 7.6: Breakdown probability according to the model in different running conditions: unloaded (left), loaded (center), antiloaded (right). The different scale has to be noted: while the breakdown probability oscillates between the 1.8% and 5% in the unloaded case, when the beam is present the difference is much bigger.

### 7.3.2 Measurement results

The breakdown distribution, cumulating the data at the same input power, are shown in Fig. 7.7. Both the linear scaling with the surface field and the scaling proposed in the precedent section are plotted.

In the centre of the structure there is a more active part, where a large number of breakdowns are happening. This active region is present both in the unloaded and loaded runs, and could be provoked by:

1. the development of an hotcell
2. surface damage of the central cells, where for some reason the surface is rougher and provokes more breakdowns.

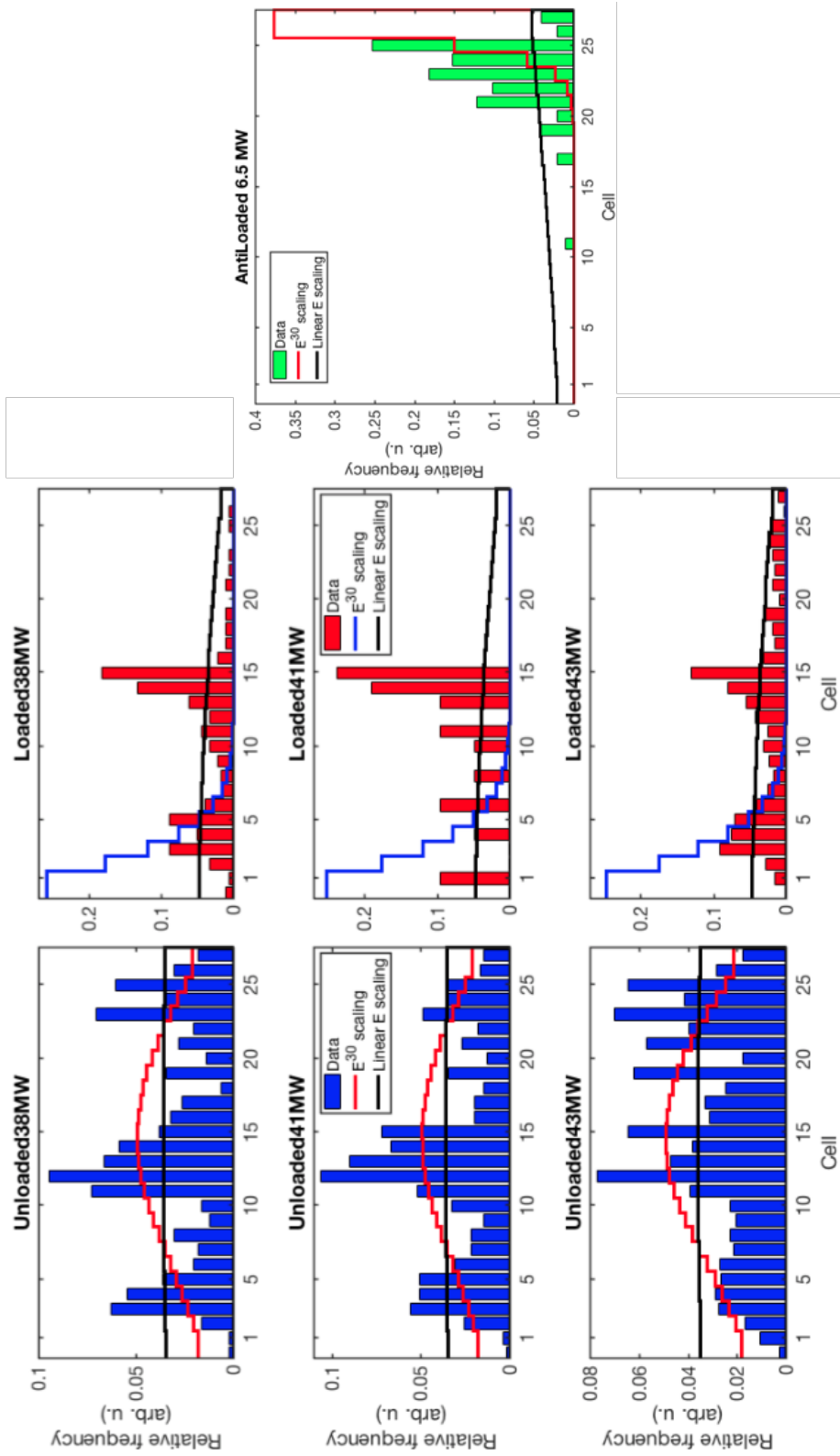


Figure 7.7: Measured breakdown distribution in the accelerating cavity under test in different running conditions. Over the data, the proposed scaling is plotted in red and the linear scaling with the surface field is plotted in black.

## CHAPTER 7. RESULTS AND FUTURE DEVELOPMENTS

---

Fortunately, there is no sign of the development of an hotcell. Figure 7.8 shows that although a warmer region in the centre developed after the antiloaded runs in June 2016, it was gradually reconditioned during the following part of the year.

Additional hints will come from the post-mortem analysis of the structure, that will be cut and examined with various microscopy techniques. This analysis will take place later in 2017. In any case, the second option looks the most probable.

The breakdown distribution is compatible with a constant distribution during runs without beam. It is also compatible with the hypothesis of accumulation of the breakdowns in the first part of the structure during the loaded runs and at the end during the antiloaded runs.

The fundamental result from this is anyway that the breakdown probability is ruled by the peak accelerating gradient, and not from the average accelerating gradient.

Even ignoring the central warm zone, it is not clear which law rules the distribution of the breakdowns in the cells. Collecting more data is necessary for this purpose.

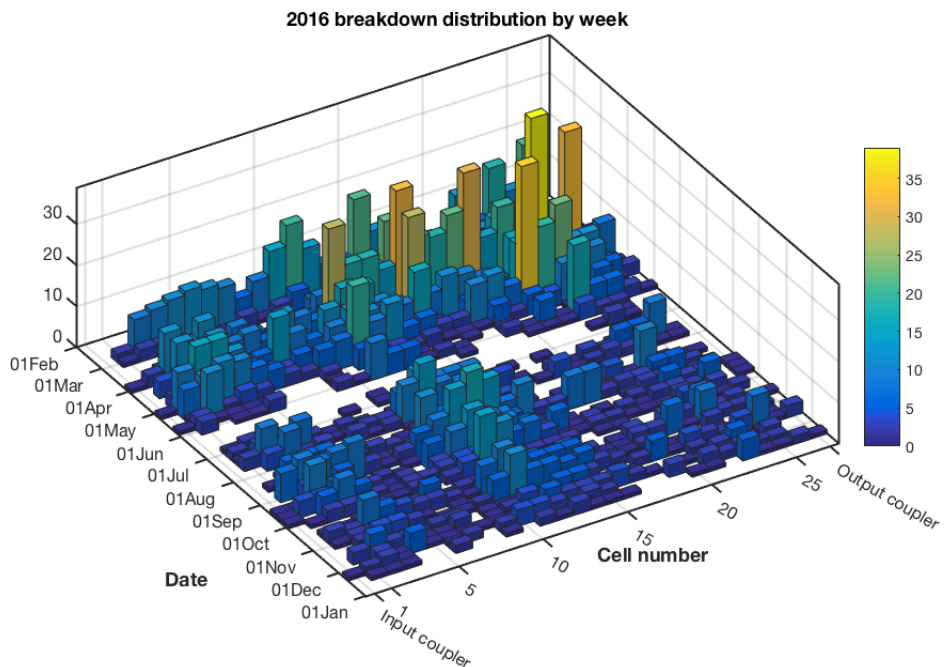


Figure 7.8: Breakdown number per cell per week.

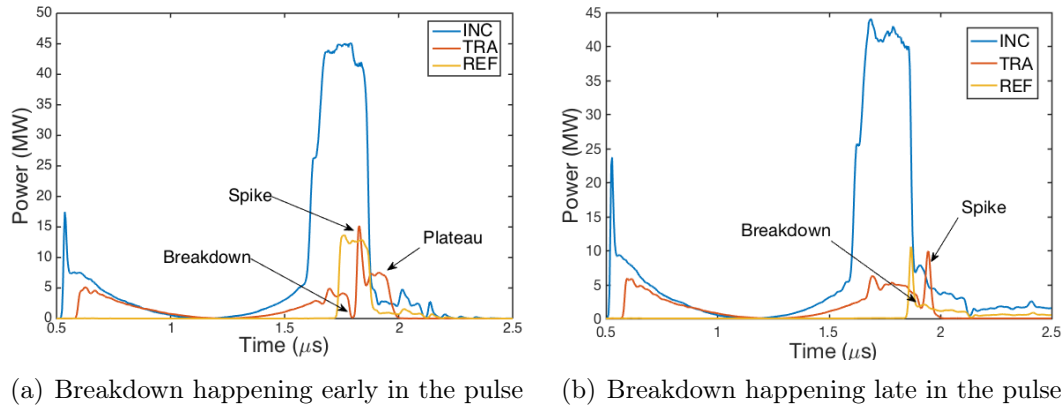
## 7.4 Beam induced RF

The effect of the beam is observable on the RF signals after a breakdown. Figure 7.9 shows two examples of RF signals. Three phases are clearly visible in the transmitted power signal:

1. the power falls after the breakdown because of the reflection of the RF caused by the plasma.
2. the beam keeps passing through the plasma. The part of the cavity after the breakdown is not filled anymore by the incident RF, and the beam starts to produce power getting decelerated. This process has a short duration and results in a spike in the power produced.
3. the power production stabilises with the establishment of a plateau in the transmitted power profile.

At the moment there is no satisfactory theory that explains the behaviour of the RF power production in the cavity after the breakdown. Hence it is not clear which process is provoking the observed power spike.

Two different examples are presented in the figure. The spike is visible on the right, but the plateau does not have time to develop because of the end of the beam pulse. On the left the full development of the process is appreciable.



(a) Breakdown happening early in the pulse      (b) Breakdown happening late in the pulse

Figure 7.9: Two examples of RF signals for a breakdown event earlier and later in the pulse. In both cases the spike provoked by the beam-induced RF production is visible. In the early case (a) it is possible to see the development of the plateau induced by the stabilisation of the power production up to the end of the beam pulse. In the late case (b) the beam pulse duration is not sufficient to allow the development of a stable condition.

## 7.5 Conclusions

The experiment described in this work offers a first glimpse on the beam effect on the breakdown rate in a normal-conducting travelling-wave accelerating structure.

During the 2016 measurement campaign, the expertise to realise breakdown experiments with the beam has been gained. The experiment were conducted with a longer beam pulse and with higher current than the CLIC Main Beam parameters to enhance the effect of the beam on the BDR.

This work showed that the breakdown rate is in general lower during experiments with the beam, performed with the same input power. This difference has to be ascribed to the internal field profile modification induced by the beam presence, which results in a lower peak accelerating gradient.

The distribution of the breakdowns in the accelerating cavity follows the field distribution, resulting in the majority of the breakdowns in the front part of the structure when accelerating the beam and in the last part when decelerating. Unfortunately, the development of an active zone in the centre of the structure makes impossible to find the scaling law for the breakdown distribution.

A different migration dynamic of the breakdowns have been detected during the loaded and antiloaded runs. This could be explained by the modified field profile induced by the loading of the cavity with the beam.

Further investigations in this field require to repeat the experiment in more stable conditions, with measurements of long duration (weeks). This last request translates into long beam times that the tight scientific program of the CTF3 was not able to provide. Missing this condition, it is not possible to understand if the continuous switching between different running conditions impacts on the fluctuation of the breakdown rate. Anyway it is reasonable to expect that this causes a higher fluctuation of the breakdown rate than the one achievable running in stable conditions.

The experiment has to be considered successful, because of the amount of information that have been collected, even with a limited and not continuous beam time in a non-dedicated experiment.

## 7.6 Further developments

The experience gained from this work allows first of all to suggest some modifications to the setup, starting by looking at the newer Xboxes:

- The substitution of the TWT with a solid state amplifier will avoid the presence of spikes. The new amplifier has been installed in XBOX1 at the beginning of 2017.
- Switching the pulse compressor from SLED-I to SLED-II type (as is in Xbox2), and placing the Xbox closer to the structure under test would

## CHAPTER 7. RESULTS AND FUTURE DEVELOPMENTS

---

solve the detuning problem (since the attenuation of the waveguides is lower and the power requested from the pulse compressor as well).

- The missing back-off in power has to be investigated and solved. Probably the performance of the interlock system program running on the FPGA could be improved by writing the related code in a hardware description language instead of LabVIEW.
- The sampling rate of the log detectors could be improved up to 1 GSa/s using the same acquisition system used for the IQ detectors.

On the physics side, pursuing the experiments in a dedicated facility would be the optimal solution. As general guideline, alternating several weeks of experiments with beam to weeks of unloaded experiments could be a good programme. This should allow to get more meaningful results and compare with the unloaded results of the Xboxes, where the normal experimental time is weeks.

Beyond the physics interest, before the implementation of CLIC, operating in the CLIC conditions would be very interesting. In this context, the comparison of the operation of the cavity at 100 MV/m average gradient would be extremely interesting.

# List of Abbreviations

BPM	Beam Position Monitor
CDR	Conceptual Design Report
CERN	Conseil européen pour la Recherche nucléaire, Geneva, Switzerland
CLIC	Compact Linear Collider
CTF3	CLIC test facility 3
EEE	Explosive Electron Emission
EFE	Enhanced Field Emission
EM	Electromagnetism -or- electromagnetic
FCC-ee	Future Circular Collider, lepton version
FCC-hh	Future Circular Collider, hadron version
FE	Field Emission
FOM	Figure Of Merit
HOM	High(er) Order Mode
ICFA	International Committee for Future Accelerators
ILC	International Linear Collider
KEK	High Energy Accelerator Research Organization, Tsukuba, Japan
LEP	Large Electron Positron Collider
LHC	Large Hadron Collider
LINAC	Linear Accelerator
LLRF	Low-level RF
NC	Normal Conducting
PETS	Power Extraction and Transfer Structure
RF	Radio frequency
SC	Super Conducting
SLAC	Stanford Linear Accelerator, Menlo Park, California
SM	Standard Model
SPS	Super Proton Synchrotron
SWS	Standing Wave Structure
TBM	Two-Beams module
TDR	Technical Design Report
TE	Transverse Electric (modes of a WG)
TM	Transverse Magnetic (modes of a WG)
TWS	Travelling Wave Structure
TWT	Travelling Wave Tube
WG	Waveguide
XBOX	X-band high power RF test stand

# List of Figures

1.1	Map of the CLIC facility, if implemented in the Geneva area. . . . .	5
1.2	Layout of the final stage of CLIC. . . . .	6
1.3	Design of a Two-beam module. . . . .	7
2.1	Scheme of a travelling wave, disk loaded accelerating structure. The drawings illustrates the input and output couplers, the disks loading the cavity and the beam passing through the irises. From [24] . . . . .	11
2.2	Brillouin diagram of a uniform waveguide (red) compared to a disk-loaded accelerating structure (green) [25] . . . . .	12
2.3	Field enhancement factors for simple geometries of metallic pro- trusions, plotted as function of geometrical features. From [29] .	16
2.4	(a) Electric field distribution around the protrusion considered. (b) Field emitted current and power flow. In both the plots arrows indicate the direction of the field and the color code the absolute value of the field, mapped logarithmically.[35] . . . . .	18
2.5	A disk composing the structure (left) and the scheme of an accelerating structure (right), including couplers for the RF, cooling elements and connection flanges. The wakefield monitor is not present in the prototype under test. . . . .	21
2.6	The structure prototype after the brazing of the copper disks and before the installation ( <i>Courtesy of A. Solodko</i> ) . . . . .	21
3.1	RF signals of a breakdown event (left) and burst of current emitted, detected by a BPM (right). The left plot shows the fall of the transmitted power (TRA) and the raise of the reflected power (REF). The RF signal of the previous pulse, without breakdown, is shown as a dashed line. Note that the time scale in the two plots are not the same. . . . .	23
3.2	Crater provoked by a breakdown in an X-band RF accelerating cavity [30] . . . . .	25
3.3	Breakdown stages in chronological order. From [25] . . . . .	26

## LIST OF FIGURES

---

4.1	Gradient profile along the TD26CC structure at 43.3 MW input power. The unloaded case and the loaded with different current intensities are shown. The average gradient difference between the adjacent curves is approximately 5 MV/m. . . . .	28
4.2	Comparison of the loaded and unloaded gradient profile of the TD26CC structure loaded with the CLIC Main Beam. When loaded with a current of 1.2 A, the input power to maintain an average gradient of 100 MV/m passes from 43.3 MW in the unloaded case to 61.3 MW in the loaded case. . . . .	29
4.3	Comparison of gradient profiles in different running conditions. The loaded and unloaded profiles are calculated at 43.3 MW input power, the antiloaded at 6.5 MW input power. The beam current in this case is 1.6 A. . . . .	30
5.1	Layout of the injector and the magnetic chicane. Legenda: SHBs: sub-harmonic bunchers. . . . .	34
5.2	Layout of the linac up to module 7. Legenda: bpm: beam position monitor. . . . .	34
5.3	Simplified layout of optics and beam instrumentation of the dog-leg line, adapted from technical drawings and facility layout [51]. The beam for this section come from the end of the module 7. Legenda: QFC(QDC): focusing(defocusing) quadrupole; DHC(DVC): horizontal(vertical) dipole corrector; BH: bending magnet in horizontal plane; BPM: beam position monitor . . . . .	35
5.4	Standalone X-band test stand layout . . . . .	36
5.5	Schematic of the high level RF and the relevant part of the DAQ for the interlock system. See appendix for glossary of abbreviations . . . . .	39
6.1	Cavity input power signal for two different spikes. Spikes can happen anytime in the signal evolution. . . . .	44
6.2	The CLIC nominal pulse and two extreme cases of detuning of the pulse compressor. . . . .	45
6.3	Metric plot for an unloaded run. Data grouped in two different regions are clearly visible. The lower-right region is containing the interesting interlocks, that are retained for the next analysis step. The thresholds are shown as red lines. . . . .	47
6.4	RF signal time delays in a travelling-wave accelerating structure. In the setup used for this experiment, the waveguide length for input and output couplers is identical and $\tau_{0,INC} = \tau_{0,TRA}$ . . . . .	49

## LIST OF FIGURES

---

6.5	RF signals of a breakdown in the structure. (a) shows the RF signals for a breakdown event, where the deviation points of the TRA and REF signals are highlighted. The dashed lines are the reference signals, given by the previous pulse. (b) is a detail of the Region Of Interest (ROI) for the correlation method marked in red in (a). The time difference between the dashed vertical lines indicate the time delay between the pattern of the signals.	50
6.6	Comparison of the signal delay distribution for the edge and correlation method in an unloaded run. 75% of the events have been retained, in the other cases the correlation method was not applicable because of the attenuation. The spike in proximity of zero in the correlation delay is visible in all datasets. . . . .	51
6.7	Comparison of edge and correlation method for the unloaded breakdowns. The straight red line represents the accordance of the two methods, the colors the number of counts per bin. . . . .	51
6.8	A possible migration scenario [70]: a) A breakdown establishes in the structure, absorbing the incident RF; b) The established arc reflects the incident RF; c) Constructive interference between reflected and incident RF provokes another arc upstream; d) As the second arc is established, any remaining power downstream is drained and the first arc gets extinguished . . . . .	52
6.9	Comparison of edge and correlation method for breakdowns in the antiloaded case. The straight red line represents the accordance of the two methods, the colors the number of counts per bin. . . . .	53
6.10	Comparison of edge and correlation method for breakdowns in the loaded case. The straight red line represents the accordance of the two methods, the colors the number of counts per bin. . . . .	53
6.11	REF signal path in the accelerating cavity . . . . .	54
7.1	Average gradient as function of the input power in different running conditions. See text for details on the measurement points. . . . .	57
7.2	Comparison of the RF signals during the loaded and antiloaded operation. During the loaded operation it can be observed that the transmitted power falls close to zero, because of the energy transferred to the beam. The opposite behaviour can be noted in the antiloaded case, where the input power is much lower than the transmitted. In this case the difference in energy is provided by the beam, that gets slowed down because of the decelerating phase of the RF. . . . .	60
7.3	History plot of the measured breakdown rate for various measurement conditions. . . . .	61

## LIST OF FIGURES

---

7.4	Comparison of the breakdown rate at different input power in three periods of stable running without altering input power. . . . .	62
7.5	Measured breakdown rate at the end of the year . . . . .	63
7.6	Breakdown probability according to the model in different running conditions: unloaded (left), loaded (center), antiloaded (right). The different scale has to be noted: while the breakdown probability oscillates between the 1.8% and 5% in the unloaded case, when the beam is present the difference is much bigger. . . . .	64
7.7	Measured breakdown distribution in the accelerating cavity under test in different running conditions. Over the data, the proposed scaling is plotted in red and the linear scaling with the surface field is plotted in black. . . . .	65
7.8	Breakdown number per cell per week. . . . .	66
7.9	Two examples of RF signals for a breakdown event earlier and later in the pulse. In both cases the spike provoked by the beam-induced RF production is visible. In the early case (a) it is possible to see the development of the plateau induced by the stabilisation of the power production up to the end of the beam pulse. In the late case (b) the beam pulse duration is not sufficient to allow the development of a stable condition. . . . .	67

# List of Tables

1.1	Comparison of two circular machines, LEP[7, 8] with FCC-ee[9, 10] with two projects for linear machines: the first and last stage of the CLIC implementation [11] and the ILC[12]	4
1.2	CLIC main parameters in the final stage	8
2.1	Parameters of the structure	20
5.1	Beam parameters used in the Dogleg [48]	32
7.1	Input power levels of measurements of 2016 measurement campaign.	58
7.2	Gradient parameters and measured breakdown rates for runs at 75 MV/m average accelerating gradient. In the last measured BDR, the error result symmetric because no missed back-off pulse was registered.	58
7.3	Gradient parameters for runs with and without beam at the same input power. $E_{\text{peak}}$ is the peak accelerating gradient.	62

# Bibliography

- [1] S. Chatrchyan *et al.*, “Observation of a new boson at a mass of 125 GeV with the CMS experiment at the LHC,” *Phys. Lett.*, vol. B716, pp. 30–61, 2012.
- [2] G. Aad *et al.*, “Observation of a new particle in the search for the Standard Model Higgs boson with the ATLAS detector at the LHC,” *Phys. Lett.*, vol. B716, pp. 1–29, 2012.
- [3] O. S. Bruening, P. Collier, P. Lebrun, S. Myers, R. Ostojaic, J. Poole, and P. Proudlock, *LHC Design Report*. Geneva: CERN, 2004.
- [4] “Icfa statement on linear colliders.” [http://icfa.fnal.gov/statements/icfa\\_lcstatement/](http://icfa.fnal.gov/statements/icfa_lcstatement/). Last accessed: 12 Dec. 2016.
- [5] A. D. Martin, W. J. Stirling, R. S. Thorne, and G. Watt, “Parton distributions for the lhc,” *The European Physical Journal C*, vol. 63, no. 2, pp. 189–285, 2009.
- [6] J. R. Ellis and I. H. Wilson, “New physics with the compact linear colider,” *Nature*, vol. 409, pp. 431–435, 2001.
- [7] S. Aull, M. Benedikt, D. Bozzini, O. Brunner, J.-P. Burnet, A. Butterworth, R. Calaga, E. Jensen, V. Mertens, A. Milanese, M. Nonis, K. Oide, N. Schwerg, L. Tavian, J. Wenninger, F. Zimmermann, L. Rinolfi, A. Blondel, M. Koratzinos, and S. Gorgi Zadeh, “Electrical Power Budget for FCC-ee,” May 2016.
- [8] P. Brown, O. C. Brunner, A. Butterworth, E. Ciapala, H. Frischholz, G. Geschonke, E. Peschardt, and J. P. H. Sladen, “Ultimate Performance of the LEP RF System,” p. 5 p, Jun 2001.
- [9] J. Wenninger *et al.*, “Future Circular Collider Study - Lepton Collider Parameters,” Tech. Rep. FCC-1401201640-DSC, CERN, Geneva, Jun 2016.
- [10] F. Zimmermann, M. Benedikt, K. Oide, A. Bogomyagkov, E. Levichev, M. Migliorati, and U. Wienands, “Status and Challenges for FCC-ee,” Tech. Rep. CERN-ACC-2015-0111, CERN, Geneva, Aug 2015.

## BIBLIOGRAPHY

---

- [11] M. Aicheler, P. Burrows, M. Draper, T. Garvey, P. Lebrun, K. Peach, N. Phinney, H. Schmickler, D. Schulte, and N. Toge, “A Multi-TeV Linear Collider Based on CLIC Technology: CLIC Conceptual Design Report,” Tech. Rep. CERN-2012-007. SLAC-R-985. KEK-Report-2012-1. JAI-2012-001, Geneva, 2012.
- [12] T. Behnke, J. E. Brau, B. Foster, J. Fuster, M. Harrison, J. M. Patterson, M. Peskin, M. Stanitzki, N. Walker, and H. Yamamoto, “The International Linear Collider - Volume 1: Executive Summary,” Tech. Rep. CERN-ATS-2013-037. ILC-REPORT-2013-040. KEK-Report-2013-1., Geneva, Jun 2013.
- [13] P. Lebrun, L. Linssen, A. Lucaci-Timoce, D. Schulte, F. Simon, S. Staines, N. Toge, H. Weerts, and J. Wells, “The CLIC Programme: Towards a Staged  $e^+e^-$  Linear Collider Exploring the Terascale: CLIC Conceptual Design Report,” Tech. Rep. CERN-2012-005, Geneva, 2012.
- [14] M. J. Boland, U. Felzmann, P. J. Giansiracusa, T. G. Lucas, R. P. Rassool, C. Balazs, T. K. Charles, K. Afanaciev, I. Emeliantchik, and Ignatenko, “Updated baseline for a staged Compact Linear Collider,” Tech. Rep. CERN-2016-004, Geneva, Aug 2016.
- [15] I. Bozovic-Jelisavcic, “CLIC Physics Overview,” Tech. Rep. CLICdp-Conf-2016-006, CERN, Geneva, Jun 2016.
- [16] P. G. Roloff, “Higgs Physics at the CLIC Electron-Positron Linear Collider,” Tech. Rep. CLICdp-Pub-2016-001, CERN, Geneva, Aug 2016.
- [17] R. Corsini, “First Full Beam Loading Operation with the CTF3 Linac,” Aug 2004.
- [18] R. Corsini, “Experimental verification of the CLIC two-beam scheme, status and outlook,” *Conf. Proc.*, vol. C1205201, p. TUOBC01. 3 p, May 2012.
- [19] M. Weiss, “Introduction to rf linear accelerators,” *CAS - CERN Accelerator school: 5th General accelerator physics course*, 1994.
- [20] T. P. Wangler, *RF linear accelerators; 2nd rev. version*. Weinheim: Wiley-VCH, 2008.
- [21] S. Humphries, *Principles of charged particle acceleration*. New York, NY: Wiley, 1986.
- [22] E. Botta and T. Bressani, *Elementi di elettromagnetismo avanzato*. Aracne editrice, 1 ed., Jan 2009.
- [23] J. D. Jackson, *Classical electrodynamics; 2nd ed.* New York: Wiley, 1975.

## BIBLIOGRAPHY

---

- [24] A. Streun, “Experimental methods of particle physics - particle accelerators. lecture slides.” <https://ados.web.psi.ch/empp-streun/empp.pdf>. Last accessed 4 Feb 2017.
- [25] J. W. Kovermann, A. Stahl, and W. Wuensch, *Comparative Studies of High-Gradient Rf and Dc Breakdowns*. PhD thesis, Aachen, Tech. Hochsch., Aachen, 2010. Presented 17 Dec 2010.
- [26] F. Tecker, “RF Systems,” *CAS - CERN Accelerator school: Introduction to Accelerator Physics 2016*, Oct 2016.
- [27] J. W. Wang and G. A. Loew, “Field emission and RF breakdown in high gradient room temperature linac structures,” in *Frontiers of accelerator technology. Proceedings, Joint US-CERN-Japan International School, Hayama and Tsukuba, Japan, September 9-18, 1996*, pp. 768–794, 1997.
- [28] R. H. Fowler and L. Nordheim, “Electron emission in intense electric fields,” *Proceedings of the Royal Society of London A: Mathematical, Physical and Engineering Sciences*, vol. 119, no. 781, pp. 173–181, 1928.
- [29] F. Rohrbach, *Sur les mécanismes qui conduisent à la formation de l'étincelle électrique à très haute tension et sous ultra-vide par la mesure des temps de retard à la disruption*. Geneva: CERN, 1971.
- [30] W. Wuensch, “Advances in the Understanding of the Physical Processes of Vacuum Breakdown,” Tech. Rep. CERN-OPEN-2014-028. CLIC-Note-1025, CERN, Geneva, May 2013.
- [31] W. D. Kilpatrick, “Criterion for vacuum sparking designed to include both rf and dc,” *Review of Scientific Instruments*, vol. 28, no. 10, pp. 824–826, 1957.
- [32] J. W. Wang, “Some problems on RF breakdown in room temperature accelerator structure: a possible criterion,” Tech. Rep. SLAC/AP-051, 1986.
- [33] A. S. Verdu, “Kilpatrick’s critereon, an historical perspective.” [http://indico.cern.ch/event/76081/contributions/2086273/attachments/1051717/1499553/Kilpatricks\\_Criterion.pdf](http://indico.cern.ch/event/76081/contributions/2086273/attachments/1051717/1499553/Kilpatricks_Criterion.pdf), December 2009. Last accessed: 31 Jan 2017.
- [34] W. Wuensch, “The Scaling of the Traveling-Wave RF Breakdown Limit,” Tech. Rep. CERN-AB-2006-013. CLIC-Note-649, CERN, Geneva, Jan 2006.
- [35] A. Grudiev, S. Calatroni, and W. Wuensch, “New local field quantity describing the high gradient limit of accelerating structures,” *Phys. Rev. Spec. Top. Accel. Beams*, vol. 12, p. 102001, 2009.

## BIBLIOGRAPHY

---

- [36] E. A. Litvinov, G. A. Mesyats, and D. I. ProskurovskiÄ, “Field emission and explosive electron emission processes in vacuum discharges,” *Soviet Physics Uspekhi*, vol. 26, no. 2, p. 138, 1983.
- [37] A. Grudiev and W. Wuensch, “Design of the Clic main Linac accelerating structure for Clic conceptual design report,” p. 3 p, Sep 2010.
- [38] A. Lunin, V. Yakovlev, and A. Grudiev, “Analytical solutions for transient and steady state beam loading in arbitrary traveling wave accelerating structures,” *Phys. Rev. Spec. Top. Accel. Beams*, vol. 14, p. 052001. 11 p, Dec 2010.
- [39] D. Alpert, D. A. Lee, E. M. Lyman, and H. E. Tomaschke, “Initiation of electrical breakdown in ultrahigh vacuum,” *Journal of Vacuum Science and Technology*, vol. 1, no. 2, pp. 35–50, 1964.
- [40] Z. Insepov, J. Norem, S. Veitzer, and S. Mahalingam, “Modeling Arcs,” Tech. Rep. arXiv:1108.0861, Aug 2011. Comments: 6 pages, 5 figures.
- [41] W. Wuensch, “High Gradient Breakdown in Normal-Conducting RF Cavities,” 2002.
- [42] R. Rajamaki, W. Wuensch, and V. Koivunen, *Vacuum arc localization in CLIC prototype radio frequency accelerating structures*. PhD thesis, Aalto U., Otaniemi, Espoo (Finland), Apr 2016. Presented 19 Jan 2016.
- [43] D. K. Davies, “The initiation of electrical breakdown in vacuum. a review,” *Journal of Vacuum Science and Technology*, vol. 10, no. 1, pp. 115–121, 1973.
- [44] A. Palaia, M. Jacewicz, T. Muranaka, R. Ruber, V. Ziemann, and W. Farabolini, “RF-Breakdown kicks at the CTF3 two-beam test stand,” p. 4 p, May 2012.
- [45] A. Degiovanni, W. Wuensch, and J. Giner Navarro, “Comparison of the conditioning of High Gradient Accelerating Structures,” Tech. Rep. CERN-ACC-2015-0139. CLIC-Note-1056, CERN, Geneva, Jun 2015.
- [46] A. Degiovanni, S. Doeberl, W. Farabolini, A. Grudiev, J. Kovermann, E. Montessinos, G. Riddone, I. Syratchev, R. Wegner, W. Wuensch, A. Solodko, and B. Woolley, “High-Gradient test results from a CLIC prototype accelerating structure : TD26CC,” p. 4 p, Jun 2014.
- [47] R. D. Ruth, “CTF3 Design Report,” Tech. Rep. SLAC-PUB-9672, Stanford, CA, 2003. Submitted on 13 Mar 2003.
- [48] J. L. Navarro Quirante, R. Corsini, A. Degiovanni, S. Döbert, A. Grudiev, O. Kononenko, G. McMonagle, S. Rey, A. Solodko, I. Syratchev, F. Tecker, L. Timeo, B. Woolley, X. Wu, W. Wuensch, O. Kononenko,

## BIBLIOGRAPHY

---

- A. Solodko, J. Tagg, B. Woolley, and X. Wu, “Effect of Beam-Loading on the Breakdown Rate of High Gradient Accelerating Structures,” p. TUPP033. 3 p, 2014.
- [49] A. D. Yeremian, R. Miller, R. D. Ruth, H. H. Braun, G. Geschonke, L. Groening, L. Rinolfi, L. Thorndahl, I. H. Wilson, and F. Zhou, “CTF3 drive-beam injector design,” Sep 2002.
- [50] H. H. Braun, R. Corsini, S. Döbert, E. Jensen, F. A. Tecker, and P. Urschütz, “Efficient long-pulse fully-loaded CTF3 linac operation,” Tech. Rep. CERN-OPEN-2006-070. CLIC-Note-697, CERN, Geneva, Nov 2006.
- [51] “Ctf3 design and layout.” <https://edms.cern.ch/ui/#!master/navigator/project?P:1972521142:1236731031:subDocs>. Last accessed: 7 Feb 2017.
- [52] F. Peauger, A. Hamdi, S. Curt, S. Doeberl, G. McMonagle, G. Rossat, K. Schirm, I. Syratchev, L. Timeo, S. Kuzikhov, A. Vikharev, A. Haase, D. Sprehn, A. Jensen, E. Jongewaard, C. Nantista, and A. Vlieks, “A 12 GHZ RF Power source for the CLIC study,” p. 4 p, May 2010.
- [53] B. J. Woolley, *High power X-band RF test stand development and high power testing of the CLIC crab cavity*. PhD thesis, Lancaster U., Aug 2015.
- [54] J. Kovermann, N. Catalan-Lasheras, S. Curt, S. Doeberl, M. Naon, G. McMonagle, E. Paju, S. Rey, G. Riddone, K. Schirm, I. Syratchev, L. Timeo, W. Wuensch, A. Hamdi, F. Peauger, J. Eichner, A. Haase, and D. Sprehn, “Commissioning of the First Klystron-Based X-Band Power Source at CERN,” *Conf. Proc.*, vol. C1205201, p. THPPC060. 3 p, May 2012.
- [55] “Applied systems engineering, inc.” [http://www.applsyst.com/pulse\\_twt.html](http://www.applsyst.com/pulse_twt.html). Last accessed: 27 Feb 2017.
- [56] “Cpi x-band klystron vkx-8311a specifications.” <http://www.cpii.com/docs/datasheets/154/VKX-8311A%20Datasheet.pdf>. Last accessed: 22 Feb 2017.
- [57] A. Fiebig and C. Schieblich, “A SLED type pulse compressor with rectangular pulse shape,” p. 4 p, Jun 1990.
- [58] A. Bogdashov, G. Denisov, S. Kuzikov, A. Vikharev, K. Schirm, and I. Syratchev, “A 12 GHz pulse compressor and components for the CLIC test stand,” *Proc. RuPAC-2010, Protvino, Russia*, p. TUPSA005. 4 p, 2010.

## BIBLIOGRAPHY

---

- [59] S. Deghaye, D. Jacquet, J. Kozar, and J. Serrano, “Oasis: A New System to Acquire and Display the Analog Signals for LHC,” p. 4 p, Nov 2003.
- [60] “National instrument pxi systems.” <http://www.ni.com/pxi/>. Last accessed: 21 Feb 2017.
- [61] E. Daskalaki, S. Döbert, M. Duquenne, H. Mainaud Durand, V. Rude, and A. Vamvakas, “Study of the Dynamic Response of CLIC Accelerating Structures,” no. CERN-ACC-2015-286, p. TUPTY003. 4 p, 2015.
- [62] “Matlab by mathworks®.” <https://www.mathworks.com/products/matlab.html>. Last accessed: 21 Mar 2017.
- [63] “National instrument tdms file format.” <http://www.ni.com/white-paper/3727/en/>. Last accessed: 6 Mar 2017.
- [64] B. Woolley, “X-band test-stand operation: Llrf, controls, conditioning and operational algorithms, stability, xbox3 schedule.” CLIC Workshop 2016.
- [65] F. Tecker. Private communication. July 2016.
- [66] A. Degiovanni, S. Döbert, W. Farabolini, I. Syratchev, W. Wuensch, J. Giner Navarro, J. Tagg, and B. Woolley, “Diagnostics and Analysis Techniques for High Power X-Band Accelerating Structures,” p. TUPP029. 3 p, 2014.
- [67] E. Alpaydin, *Introduction to machine learning*. MIT press, 1 ed., 2004.
- [68] W. Wuensch. Private communication. March 2017.
- [69] M. Jacewicz, “Breakdown tomography with emitted electrons.” CLIC Workshop 2016.
- [70] A. Degiovanni, W. Farabolini, and al., “Breakdown position analysis.” International Workshop on Breakdown Science and High Gradient Technology (HG2015).
- [71] N. Shipman, W. Wuensch, and R. Jones, *Experimental study of DC vacuum breakdown and application to high-gradient accelerating structures for CLIC. Vol. 35 - Experimental study of DC vacuum breakdown and application to high-gradient accelerating structures for CLIC*. PhD thesis, Manchester U., Geneva, Nov 2015. Presented 11 Dec 2014.
- [72] N. Shipman, S. Calatroni, R. M. Jones, and W. Wuensch, “Measurement of the dynamic response of the CERN DC spark system and preliminary estimates of the breakdown turn-on time,” *Conf. Proc.*, vol. C1205201, p. THPPC027. 3 p, May 2012.
- [73] A. Grudiev. Private communication. March 2017.